SYSTEMS BIOLOGY

Polysome propensity and tunable thresholds in coding sequence length enable differential mRNA stability

Sayanur Rahaman, Simone Faravelli†, Sylvia Voegeli†, Attila Becskei*

The half-life of mRNAs, as well as their translation, increases in proportion to the optimal codons, indicating a tight coupling of codon-dependent differential translation and degradation. Little is known about the regulation of this coupling. We found that the mRNA stability gain in yeast depends on the mRNA coding sequence length. Below a critical length, codon optimality fails to affect the stability of mRNAs although they can be efficiently translated into short peptides and proteins. Above this threshold length, codon optimality–dependent differential mRNA stability emerges in a switch-like fashion, which coincides with a similar increase in the polysome propensity of the mRNAs. This threshold length can be tuned by the untranslated regions (UTR). Some of these UTRs can destabilize mRNAs without reducing translation, which plays a role in controlling the amplitude of the oscillatory expression of cell cycle genes. Our findings help understand the translation of short peptides from noncoding RNAs and the translation by localized monosomes in neurons.

INTRODUCTION

The expression of a gene can be tuned by a single factor controlling more than one of the processes involved in mRNA and protein turnover. For example, many of the highly expressed genes have a marked codon bias, and optimal codons are typically decoded by abundant tRNAs (*1*). The efficient decoding permits fast translational elongation, which at the same time stabilizes mRNAs and consequently, mRNAs enriched in optimal codons have typically longer half-lives (*2, 3*). Thus, the dual effect of codon optimality on translation and mRNA degradation results in a multiplicative gain in gene expression.

The linear relationship between codon composition and mRNA half-lives can explain around half of the variance in mRNA half-lives (*4*). Thus, codon optimality is a major determinant of differential mRNA stability, a term we will use in this sense in this work. There are however classes of mRNAs whose half-life cannot be explained by the standard model. For example, it has been noticed that mRNAs with short coding sequences (CDS) have shorter-than-expected half-lives; these mRNAs are enriched in the monosomal fraction, when mRNAs are separated according to the number of ribosomes translating them (*5*). The exploration of this process in detail is challenging because both optimal codon-poor and optimal codon-rich mRNAs have similar polysome profiles (*3*). Consequently, mRNAs have similar ribosome density regardless of their optimal codon content. Nonlinear effects in mRNA stability have been also observed when canonical start codons were eliminated: The elimination of start codons does not always lead to destabilization of mRNA; some of them may get stabilized (*6*). These findings suggest that there is a coupling between translation and mRNA degradation; however, this coupling may be nonlinear or unpredictable in certain classes of mRNAs. In this work, we identified conditions underlying this coupling in the eukaryotic model organism *Saccharomyces cerevisiae*.
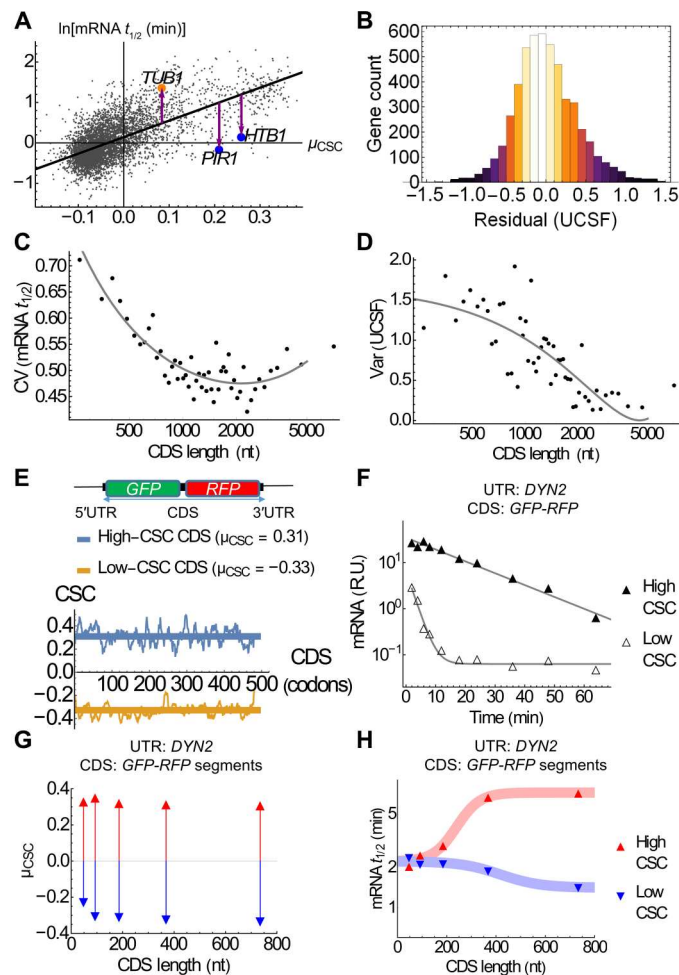
RESULTS

Differential mRNA stability emerges above a threshold in coding sequence length

The study of mRNA stability determinants requires an accurate half-life dataset. In the absence of a golden standard, averaging datasets from different studies can be used to filter out systematic measurement noise. Such an approach has been used, for example, to obtain reliable protein concentration estimates from proteomic datasets (*7*). We collected half-life datasets that display positive inter-method correlation with the aim to minimize bias due to method-specific measurement noise. Specifically, each dataset had to have at least one instance of a sufficiently high interclass correlation, defined as $r_s > 0.3$ between the following method classes: transcriptional inhibition, metabolic labeling, or genomic run-on (Materials and Methods and fig. S1A). We normalized each dataset by its median and calculated the average mRNA half-life. Subsequently, we compared the resulting unified half-lives to a dataset obtained with a fourth independent method, the multiplexed gene control (fig. S1B). The unified dataset obtained with simple averaging correlated strongly with the gene control datasets, $r_s = 0.86$ to 0.90. When the averaging was performed after outlier data of each gene were removed using the median absolute deviate (MAD)–based trimming, the correlation improved further to 0.92 (figs. S1B and S2A). Therefore, we used the MAD-based trimming to construct the unified high-precision mRNA half-life dataset.

The stabilization of mRNAs by codons can be quantified with the coefficient of correlation between the frequency of a particular codon in mRNAs and the mRNA half-life. This coefficient is also termed the codon stability coefficient (CSC) (*3*). The average CSC (μ_{CSC}; Materials and Methods and data S1) of an mRNA reflects the overall contribution of codons to its half-life. The strong correlation between the μ_{CSC} and the unified half-lives ($R^2 = 0.45$) confirms the major effect of codon composition on mRNA stability. We fitted a first order linear function to these two variables with linear regression and calculated the residual, the distance between the regression function, and the unified mRNA half-life of each mRNA (Fig. 1A). This residual comprises all stabilizing and destabilizing activities beyond the linear effects of codons (Fig. 1, A and B). We termed

Biozentrum, University of Basel, Spitalstrasse 41, 4056 Basel, Switzerland.
*Corresponding author. Email: attila.becskei@unibas.ch
†These authors contributed equally to this work.

Fig. 1. Variation of mRNA stability due to codon composition and CDS length.
(**A**) The logarithm of the (MAD trimmed) unified mRNA half-lives was used for the fitting of the function $\ln[t_{1/2}] = Y = 0.14 + 4.07\mu CSC$ (black line) with linear regression. The residual is the vertical distance between the function and the unified mRNA $t_{1/2}$. Positive (*TUB1*) and negative residuals (*HTB1* and *PIR1*) are indicated by upward and downward arrows, respectively. $N = 5151$. (**B**) The distribution of residuals (UCSF) across the transcriptome. (**C**) The coefficient of variation (CV) of half-lives in ordered bins of 100 mRNAs grouped according to coding sequence length. All eight high-throughput datasets were combined to calculate the CV. The Spearman rank correlation is $r_S = -0.52$. (**D**) Variance of UCSF in ordered bins of 100 mRNAs, $r_S = -0.82$. (**E**) The CSC profiles of the coding sequences containing a tandem fluorescent reporter construct. The thin line is the moving average of the CSC across 10 codons, and the thick line is the overall average (μ_{CSC}) of the entire CDS (491 codons including start and stop codons). (**F**) Decay kinetics of the mRNAs [in relative units (R.U.)] comprising the *DYN2* UTRs and CDS encoding the tandem reporters. (**G**) μ_{CSC} of the CDSs with different lengths derived from the low-CSC (blue downward triangles) and high-CSC (red upward triangles) series of mRNAs. (**H**) The half-lives measured for the CDS series shown in (G). Curves denote Eq. 5 fitted to data with parameters ± SE: $L_c = 267 \pm 14$ nt, $k = 0.021 \pm 0.003$, $V_n = 5.0 \pm 0.1$ min for high CSC; $L_c = 400 \pm 85$ nt, $k = 0.012 \pm 0.013$, $V_n = -0.8 \pm 0.1$ min for low CSC.

this residual the ultracodonic stabilization factor (UCSF) since it includes noncodonic effects, nonlinear effects of codon combinations, unexplained control of mRNA stability, and residual measurement noise. A nonlinear codonic effect could arise, for example, due to codon adjacency. Some adjacent codons affect translation in a codon-order specific way (*8*). A similar codon-order related effect on mRNA stability would not be captured by the μ_{CSC} because it is a linear scalar product of codon frequency and CSC.

The half-lives in the datasets become more variable with decreasing coding sequence length, especially when the length is less than 750 nucleotides (Fig. 1C), and therefore, the predictions become more limited. Similarly, the UCSF is more variable in the groups of short genes (Fig. 1D and fig. S2B). It is difficult to make reliable predictions for short genes given the high measurement noise and frequent ultracodonic effects in them. Therefore, we sought to explore experimentally how gene length affects the codon dependence of the mRNA stability.

We created an open reading frame (ORF) encoding a tandem of fluorescent proteins [green fluorescent protein (GFP) and red fluorescent protein (RFP)]. The resulting coding sequence (1.5 kb) has a length similar to the average in the yeast genome (1.2 to 1.3 kb). Two variants of the coding sequence (CDS) were constructed, one enriched in stabilizing codons [high CSC, *GFP(S)-RFP(S)*] and the other one in destabilizing codons [low-CSC, *GFP(U)-RFP(U)*] (Fig. 1E). The ORF was flanked by the untranslated region (UTR) of the dynein 2 (*DYN2*) gene, which has a relatively short CDS (279 nt). We measured the half-lives with multiplexed gene control (Materials and Methods). The low and high-CSC mRNAs yielded half-lives of 1.4 and 11.3 min (Fig. 1F), respectively, confirming the role of codon optimality.

Next, we segmented the tandem reporter to create shorter ORFs of various lengths. The lengths of ORFs ranged from 48 nucleotides (16 codons including start and stop codons) to 735 nucleotides, with a distinctively low or high mean CSC in the two series (Fig. 1G). The half-lives of the mRNA with shortest CDSs (16, 31, and 62 codons) were very similar regardless of codon composition and were short at about 2 min. In general, mRNAs with short coding sequences failed to respond to codon composition (Fig. 1H). It is unexpected that no differential half-lives were observed between the low and high CSC series because the differences in the codon optimality are substantial, also in comparison to the full range of genome-wide μ_{CSC} values (Fig. 1A).

Large differences in the half-lives arose above a threshold length, between 200 and 350 nucleotides. In particular, high-CSC mRNAs got increasingly stable with the CDS length, but a minor destabilization of low-CSC mRNAs was also observed in longer CDSs (Fig. 1H).

UTRs can tune the threshold length for differential mRNA stability

The combined responses of the low- and high-CSC mRNAs result in a switch-like emergence of differential half-life (Fig. 2A). To explore this switch-like response in more detail, we varied the UTRs and added a sequence tag [nano-luciferase complementing peptide (nLCP)] to the ORF that can be used for protein quantification by complementation. We have chosen the *RPL41A* UTR, which is naturally adapted to short ORFs since Rpl41a is a ribosomal microprotein, comprising only 25 amino acids. The half-lives converged to identical values as the CDS length was shortened in
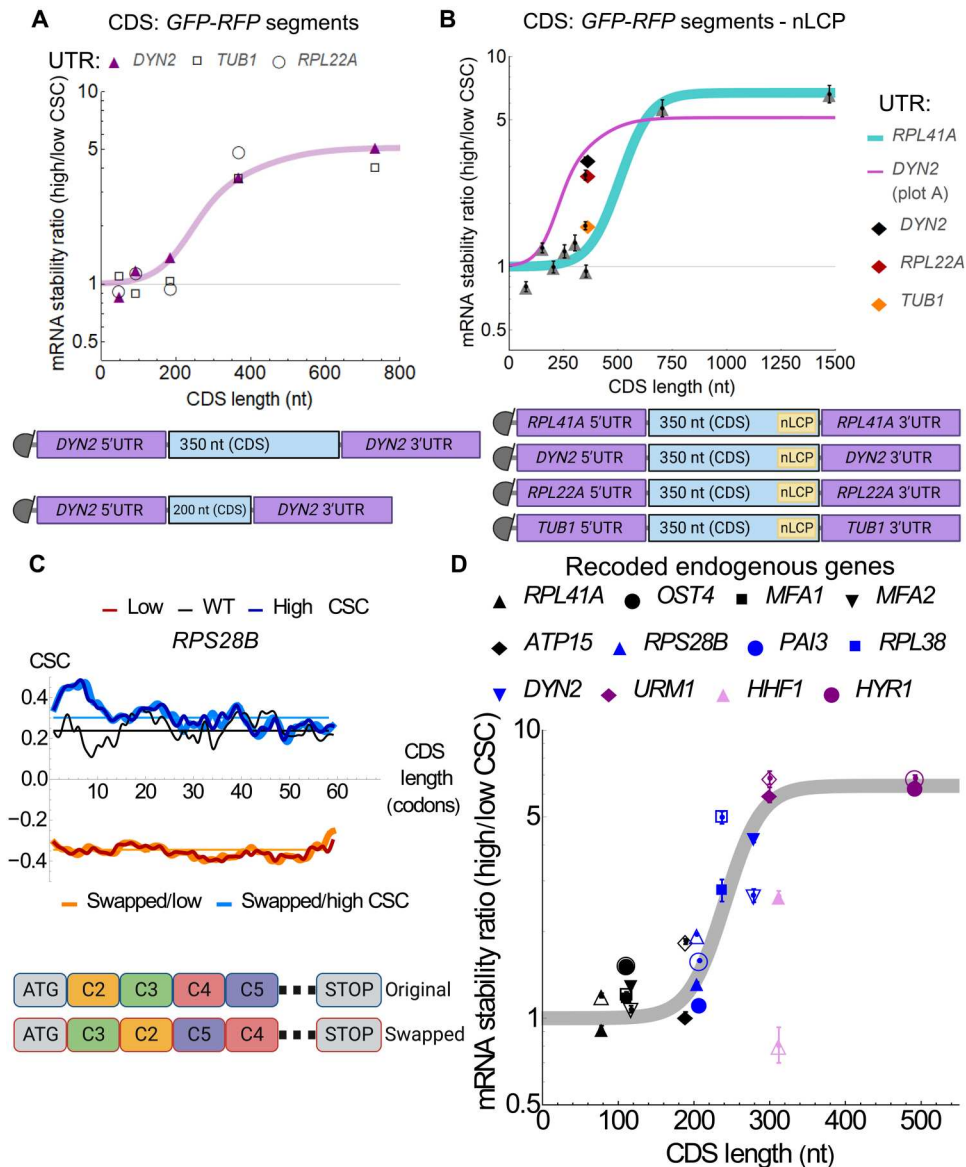
Fig. 2. The length dependence of differential mRNA stability. (**A**) Differential mRNA stability of the mRNAs with the indicated UTRs and the CDS segments derived from the tandem reporter genes. The half-life ratio of *DYN2* UTR mRNAs with high- and low-CSC are calculated from Fig. 1H. The purple curve is the ratio of the fitted functions in Fig. 1H. (**B**) The half-lives of the mRNA series with the nLCP peptide. Eq. 6 (cyan) fitted to the half-lives of mRNAs with *RPL41A* UTR (gray triangles, SE, *N* = 3). Fitted parameters ± SE: L_c = 572 ± 31 nt, *k* = 0.015 ± 0.002, V_r = 5.72 ± 0.21. The spread of half-lives of the 354/363 nt CDS due to the variation of UTRs is shown with diamonds. (**C**) The CSC profiles of the recoded *RPS28B CDS*. The thick lines denote the moving average of the CSC across 10 codons, and the thin lines denote the μ_{CSC} of the entire CDS. The thick black line stands for the endogenous WT gene. (**D**) The filled symbols denote the mRNA stability ratio of the recoded original endogenous genes (high to low CSC), whereas the corresponding empty symbols denote the ratios calculated for the codon swapped versions of the CDS. Error bars: SE (*N* = 3). The curve denotes Eq. 6 fitted to data represented as filled symbols except for *HHF1*. Fitted parameters ± SE: L_c = 262 ± 6 nt, *k* = 0.044 ± 0.007, V_r = 5.41 ± 0.35.

this case, as well. The response can be fitted well with a sigmoidal function that describes a first order reaction along the mRNA, which takes place proportionally to the distance covered by the translating ribosomes (Materials and Methods). Unexpectedly, the threshold length increased to between 350 and 700 nt (Fig. 2B) despite the *RPL41A* UTR's original association with short CDS. The increase in the threshold can arise due to the UTR or the nLCP sequence. We tested three additional UTRs in the context of the approximately 350-nt-long CDS.

In contrast to *RPL41A* UTR, differential half-life was observed with all of them, especially with the *DYN2* and *RPL22A* UTRs, resulting in an around threefold modulation of differential stability by UTRs, which suggests that UTRs can modulate the half-life in the vicinity of the threshold. At the same time, the mRNA stability ratio of the mRNAs with the *TUB1* UTR was higher when the nLCP tag was absent (cf. Fig. 2, A and B, and data S4). This suggests that the change in coding sequence, due to the nLCP tag, rich in positively charged amino acids (Lys and Arg), can also shift the threshold.

Type II UTRs suppress differential mRNA stability even in long coding sequences

To test whether the endogenous mRNAs behave similarly, we recoded the coding sequence of 12 mRNAs ranging in length from 78 to 492 nt with either optimal or non-optimal codons (Fig. 2C, fig. S3A, and data S5). No or minimal difference in stability was observed for shorter mRNAs with a CDS of up to 200 nt, namely, the *RPL41A*, *OST4* (subunit of translocation complex in the endoplasmic reticulum), the mating factor A (*MFA1* and *MFA2*), and *ATP15* (subunit of the mitochondrial ATP synthetase) mRNAs (black symbols in Fig. 2D). An increasing difference in stability was observed for CDSs between 200 and 300 nt (blue symbols in Fig. 2D), namely, the *RPS28B*, *RPL38* (subunits of the ribosome), *PAI3* (proteinase A inhibitor), and *DYN2* mRNAs. The mRNA stability ratio reaches high values for CDS longer than 300 nt, such as *URM1* and *HYR1*, with the exception of *HHF1*, a histone mRNA.

Altered codon optimality can change protein abundance, which can lead to indirect changes in mRNA stability. For example, the overexpression of Rps28 protein accelerates the degradation of its own (*RPS28B*) mRNA through a UTR-mediated feedback loop (*9*). To detect possible indirect changes in mRNA stability due to feedback loops, we created swapped versions of the recoded sequences in which every odd codon was swapped with the adjacent even codon. This swapped version retains the exact codon composition and the CSC moving average along the sequence (Fig. 2C). At the same time, it makes the protein nonfunctional, eliminating possible feedback loops.

The overall trend of increasing mRNA stability ratios with CDS length recapitulates the findings with the recoded original mRNAs (empty versus filled symbols in Fig. 2D). This length dependence threshold observed with endogenous mRNAs is in close agreement with the findings with the reporter gene segments. Thus, the large variability of UCSF of short genes (Fig. 1D) reflects in part the absent or decreased codon dependence of shorter mRNAs.

Small but significant differences in the stability ratios of the original and the swapped recoded mRNAs were seen for most mRNAs with CDS between 200 and 300 nt, including the *RPS28B*. In the case of *RPS28B*, the difference was largely due to a 0.7-fold lower stability of the high-CSC mRNA in comparison to its swapped counterpart (paired *t* test, *P* value = 0.003). These differences may indicate a negative feedback loop. Alternatively, differences in the half-lives of the swapped and original CDSs can arise due the specific codon order, as well. The *HHF1* displayed the largest difference in the mRNA stability ratios; the half-life of the high-CSC mRNA was 2.6-fold higher than that of its swapped counterpart (paired *t* test, *P* value = 0.002). This suggests that the histone overexpression from the high-CSC mRNA triggers a feedback loop that stabilizes the mRNA directly or indirectly through changes in the cell cycle (*10*, *11*). The swapped versions of the *HHF1* mRNA did not display differential stability despite the relatively long coding sequence.

To investigate why the *HHF1* mRNA does not display differential stability, we fused the *HHF1* UTR to the CDS containing the *GFP-RFP* segments and the nLCP. The half-lives of the resulting high-CSC mRNAs were very short (1 to 2 min) and similar or even lower than the half-lives of the low-CSC mRNAs, showing that codon optimality fails to generate differential mRNA stability over the entire range of examined CDS lengths up to 700 nt

(Fig. 3A). This result suggests that the lack of differential stability in the swapped recoded *HHF1* is due to the *HHF1* UTR.

In summary, there are two classes of UTRs that act differently. Type I UTRs have a major effect on differential mRNA stability only close to the threshold length. Thereby, they tune the threshold length (Fig. 3B). On the other hand, type II UTRs destabilize mRNAs both at and above the threshold length.

Omitting the *HHF1*, whose UTR is categorized as type II, we fitted Eq. 6 to the stability ratios of all other recoded mRNAs (Fig. 2D and fig. S3B). The fitted threshold lengths for the original endogenous mRNAs, L = 262 nt, and their swapped counterparts, L = 256 nt, were similar. They fall in the same range as the threshold length fitted for the reporter segments (Fig. 2A).

UCSF helps identify type II (destabilizing) UTRs

The histone *HHF1* has a strongly negative UCSF (−0.98). We performed an enrichment analysis of genes with extreme UCSF values: Nucleosome (histone genes) and the cell wall were the most enriched cell components (fig. S4A). Among the histone genes, 6 were among the 200 genes with the most negative UCSFs and were detected independently of the exact procedure of the calculation of unified half-lives (fig. S4, B and C): *HHF1*, *HHF2*, *HHT1*, *HTA1*, *HTB1*, and *HTB2*. The histone mRNAs are rich in stabilizing codons, and their expression oscillates with large amplitude in the cell cycle, with peak levels in the S-phase (*11*, *12*).

Given the marked oscillatory expression of the histone and cell wall genes, we wondered as to whether other cell cycle genes show a similar enrichment (see Materials and Methods). Genes with the strongest oscillations have more negative UCSF than the genes with weaker or no cell cycle oscillations (Fig. 3C). Specifically, the mean UCSF of the 150 most (blue tilde) and least (blue line) periodic genes is −0.27 and 0.12 (*P* value = 8×10^{-15}, Mann-Whitney *U* test). This indicates that ultracodonic mRNA destabilization plays an important role in the oscillatory gene expression program of the cell cycle.

To explore whether specific degradation pathways mediate this ultracodonic destabilization, we compared the UCSF with the destabilization by nonsense mediated decay (NMD). NMD is triggered by premature stop codons, for example, in the form of small ORFs upstream of the main ORF or by long 3′UTRs. NMD can also arise due to sequences in the mRNA that increase the probability of ribosomal frameshifting in the coding sequence (*13*). Thus, the negative UCSF may originate in the UTR as well as in the coding sequence. An analysis of half-lives measured in Δ*upf3* cells (*14*), which are deficient in NMD, reveals that mRNAs subject to a larger than threefold destabilization by NMD have an average UCSF of −0.34, showing that NMD is an important contributor to ultracodonic destabilization (Fig. 3D). However, among the 100 genes with most strongly oscillating expression, only two genes are affected by NMD; thus, NMD is not a major contributor to ultracodonic effect in the cell cycle genes.

Since UTRs are important mediators of regulation of translation and degradation (*15*, *16*), we wondered whether some of the genes with extreme UCSF values encode UTRs that modulate mRNA stability. In the distribution of the residuals, the bottom and top 2.5 percent of the genes have a UCSF less than −0.72 and more than 0.87, respectively (Fig. 1B). *PIR1* (encoding a cell wall protein) has a UCSF = −1.15, and *TUB1* (tubulin 1) has a UCSF = 0.88 (Fig. 1A), exemplifying mRNAs with extreme UCSF values.
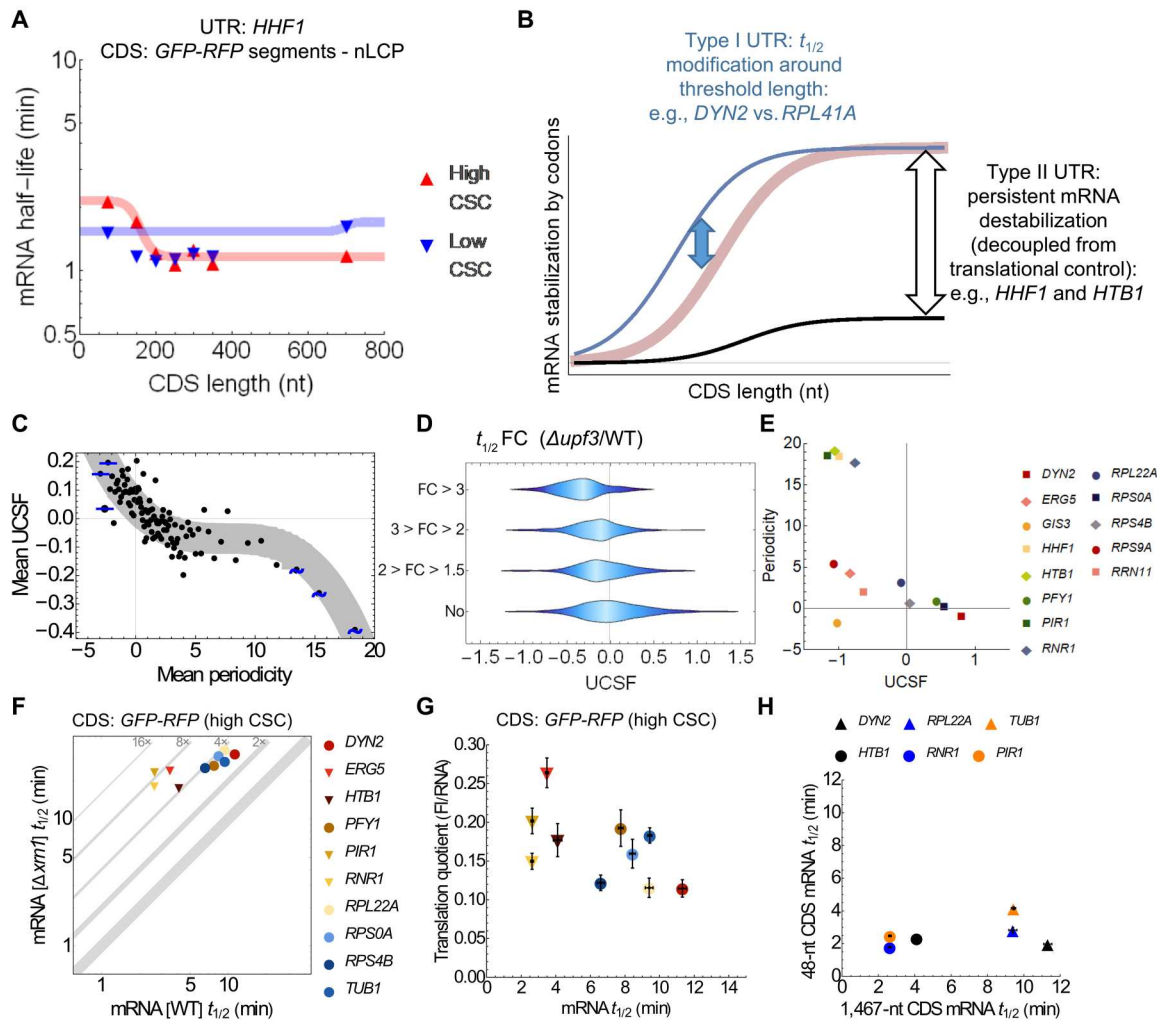
Fig. 3. Type II UTRs can decouple mRNA stability from codon optimality and translation. (**A**) The half-lives of mRNAs with the *HHF1* UTR and the CDS series encoding the tandem reporter segments and with the nLCP tag. (**B**) Scheme of UTR classes. Type II UTRs destabilize mRNAs without reducing translation, thus they decouple codon optimality–dependent translation from RNA degradation. (**C**) Each circle represents the mean UCSF of ordered bins of 50 mRNAs ranked by the periodicity of mRNA expression. The periodicity is the negative logarithm of the *P* value of periodicity of gene expression in synchronized yeast cells (*50*). (**D**) Fold change (FC) in half-life due to the deletion of *UPF3*. mRNAs that get stabilized upon *UPF3* deletion have a significantly lower UCSF in comparison to nonresponding mRNAs. Specifically, mRNAs with FC > 3 (*N* = 46): mean UCSF = − 0.34, *P* value = 3.6×10^{-11}; FC > 2 (*N* = 249): mean UCSF = −0.2, *P* value = 3.4×10^{-22}. mRNAs with FC < 1.5 (*N* = 4607) have a mean UCSF = 0.02. Mann-Whitney *U*. (**E**) The periodicity and UCSF of the genes whose UTRs were tested in this study. (**F**) The half-life of mRNAs (*n* = 2) containing the tandem reporter ORF flanked by the indicated UTRs measured in WT and Δ*xrn1* cells. (**G**) Translation quotient measured based on GFP fluorescence as a function of mRNA half-life of the series shown in (F). UTRs obtained from genes with positive and negative UCSF are indicated by circles and triangles, respectively. Error bars: SE (*N* = 4). (**H**) Half-lives of high-CSC mRNAs with long (1467 nt) or short (48 nt) coding sequence flanked by UTRs with positive (triangles) and negative UCSF (circles). The long mRNAs encode the tandem GFP-RFP (SE; *N* = 3).

We fused the *TUB1* and *PIR1* UTRs to the ORF with the tandem reporter gene. The mRNA comprising the *TUB1* UTR and *GFP(S)-RFP(S)* CDS had a relatively long half-life (9.4 min; fig. S5). When the *PIR1* UTR was fused to the same CDS, the half-life was reduced nearly fourfold (to 2.6 min). Thus, UCSFs were mediated by the UTRs. The half-lives of the mRNAs enriched in destabilizing codons [*GFP(U)-RFP(U)* CDS] were similarly short, irrespective of the UTR (1.0 and 1.1 min). In other words, UCSF can be used to help the detection of UTRs modulating mRNA stability, but their effect was observed only in the context of optimal codons, in the form of mRNA destabilization.

We extended the above tandem-reporter series with UTRs of genes with negative UCSF whose expression was either highly periodic (*PIR1*, *HTB1*, and *RNR1*) or weakly periodic (*ERG5*) (Fig 3, E and F) across the cell cycle. None of these genes is subject to NMD. As control, we have taken UTRs from RNAs both with positive UCSF, with high and low cell cycle periodicity. Despite the high proportion of optimal codons in the tandem reporter, the mean half-life of the mRNAs with the UTRs obtained from genes with negative UCSF (triangles, 3.2 min) is significantly shorter than that of those with positive UCSF (circles, 8.8 min); *P* value = 0.014 (Mann-Whitney *U*) (Fig. 3F).

This destabilization by the UTRs is dependent on the Xrn1 exoribonuclease, which degrades mRNAs in a 5′-to-3′ direction (*17*), as evidenced by the around eightfold stabilization of *GFP(S)-RFP(S)* mRNAs in Δ*xrn1* cells, in comparison to fourfold stabilization with UTRs from positive UCSF. Nonetheless, the destabilizing UTRs promote a faster decay even in Δ*xrn1* cells, suggesting that they are subject to an Xrn1-independent pathway, as well. When the UTRs flank a low-CSC CDS, all mRNAs undergo an around 16-fold stabilization in Δ*xrn1* cells, independently as to whether the UTRs derived from genes with positive or negative UCSF. This observation underscores that these UTRs have little or no effect in the context of the sequences with low codon optimality (fig. S6C). Regardless of the exact sequence or type of the UTRs, all half-lives converge to relatively short values as the CDS length decreases (Fig. 3H).

Type II UTRs decouple translation and mRNA degradation, allowing efficient translation of short-lived mRNAs

Given the coupling between translation and mRNA stabilization (*18*), we wondered whether the destabilization by the UTR entails reduced translation. Therefore, we measured the fluorescence of proteins translated from the UTR–tandem *GFP-RFP* constructs (Fig. 3G and fig. S6, A and B). Unexpectedly, the translation quotient, defined as the ratio of steady-state fluorescence to mRNA, was similar across all UTRs. Moreover, higher translational efficiency was observed with some of the UTRs associated with negative UCSF than with positive UCSF. These observations suggest that translation is decoupled from the mRNA-destabilizing effect of the UTR. This decoupling enables efficient translation of short-lived mRNAs, meeting the dynamic requirements of highly expressed cell cycle genes.

Type II UTRs enhance the amplitude of the cell cycle oscillations by mRNA destabilization

In principle, type II UTRs in the context of periodically expressed mRNAs can cause destabilization either constantly or periodically in specific phases of the cell cycle. To distinguish these possibilities, we measured decay in two different phases of the cell cycle, either in the early S phase (arrest with hydroxyurea) or in the G_2/M phase (arrest with nocodazole) (Fig. 4, A and B). The half-lives of the *GFP-RFP* CDS with various UTRs were similar in both cell cycle phases, with a slightly faster degradation in G_2/M phase in the case of *HTB1* and *PFY1* UTRs. Thus, the three- to fourfold destabilization by most type II UTRs (*PIR1*, *ERG5*, and *RNR1*) is constant across the cell cycle, and one of them, the *HTB1* UTR, profits from an additional, small cell cycle–specific acceleration of degradation.

The fast degradation the type II UTRs confer to mRNAs is advantageous to cell cycle genes because it increases the amplitude of the cell cycle oscillations in kinetic models (Fig. 4C and fig. S7C) (*17*, *19*). We tested these predictions experimentally by replacing the 3′UTRs of the *HTB1* histone gene by dynein *DYN2* UTR and the histone *HHF1* UTRs, as a positive control. The *HTB1* (CDS):: *HHF1* (UTR) displayed large amplitude oscillations during the cell cycle similar to the endogenous histone *HTA1* mRNA (Fig. 4D). Conversely, the amplitude reduced around 3.8 times with the *DYN2* UTR. This confirms that the acceleration of the histone mRNA degradation by the 3′UTR increases the amplitude of oscillatory mRNA expression.

Are there distinctive features of type II UTRs? To answer this question, we examined the proteins shown to bind to mRNAs analyzed in this study (*PIR1*, *RNR1*, *ERG5*, *HTB1*, *GIS3*, *RPS9A*, *RRN11*, and *HHF1*) in published datasets (*20*). A preliminary screen indicated their association with two RNA binding proteins, Whi3 and Puf4. A detailed analysis shows that Whi3 motifs and Whi3 high confidence targets are strongly associated with mRNAs having negative UCSF values (fig. S7A). Similarly, Puf4 binding (class 1 targets) is associated with negative UCSF (fig. S7B). Whi3 is a cell cycle regulator and also affects the stability of a cyclin mRNA (*21*). *GIS1* is a high-confidence Whi3 target and has a strongly negative UCSF (data S1). To test its role, we deleted *WHI3* to assess the change in stability of the *PDB1* (CDS) : *GIS3* (UTR) hybrid RNA. The half-life increased 1.9 times upon deletion, which is significantly higher than that of the control mRNA [*PDB1* (CDS) : *RPS9A* (UTR); 1.3 times] (fig. S7D).

It is interesting to note that 41 of the 100 mRNAs with the most negative UCSF are targets of Upf3, Whi3, or Puf1 (data S1). In contrast, only a single mRNA out of the 100 mRNAs with the most positive UCSF is a target of Upf3, Whi3, or Puf1. Thus, specific mRNA binding proteins are likely mediators or the negative UCSF and mRNA destabilization.

Type II UTRs affect mRNA stability as a nonlinear function of codon optimality

To understand the extent to which the type II UTRs can destabilize mRNAs, we created a large number of chimeric constructs by combining the coding sequences and the UTRs of endogenous genes. When various UTRs were fused to coding sequences rich in optimal codons, *PDB1* ($\mu_{CSC} = 0.15$), *PST2* ($\mu_{CSC} = 0.20$), or *RPS9A* ($\mu_{CSC} = 0.24$), strong destabilizing effect was observed with UTRs derived from genes with strongly negative UCSF (Fig. 5A). As the UCSF increased from zero to positive values, the effect of the UTRs tapered off. This is in agreement with the positive correlation between the UCSF and the relative error of half-life prediction ($r = 0.47$, $N = 105$; data S3). Therefore, a large proportion of strongly negative UCSF values are likely to be due to destabilizing UTRs, allowing for targeted screening for UTRs. The endogenous UTR of *RPS9A*, encoding a subunit of the small ribosomal protein, is strongly destabilizing despite the fact that ribosomal proteins are typically highly expressed.

In the second set of constructs, we have chosen the *RRN1* and *RPS22A* UTRs and fused them to coding sequences with a broad μ_{CSC} range. With the *RPS22A* UTR (UCSF = −0.20), the mRNA stability is increasing in proportion with the codon optimality (Fig. 5B), which fits well the linear model that was used to calculate the residuals (UCSF). On the other hand, the half-lives were relatively uniform with the *RRN11* UTR (UCSF = −0.63). They were short, between 1 and 2 min, irrespective of the μ_{CSC} of the CDS. In this case, a simple linear model does not explain the behavior of the strongly destabilizing UTR (Fig. 5B, purple dashed lines) because mRNAs rich in low-CSC codons are not destabilized considerably. Conversely, a nonlinear model that includes a multiplicative interaction of the UTR and coding sequence fits the data well (Fig. 5B, solid lines). Thus, type II UTRs reduce differential stability by nonlinearly counteracting codon optimality.
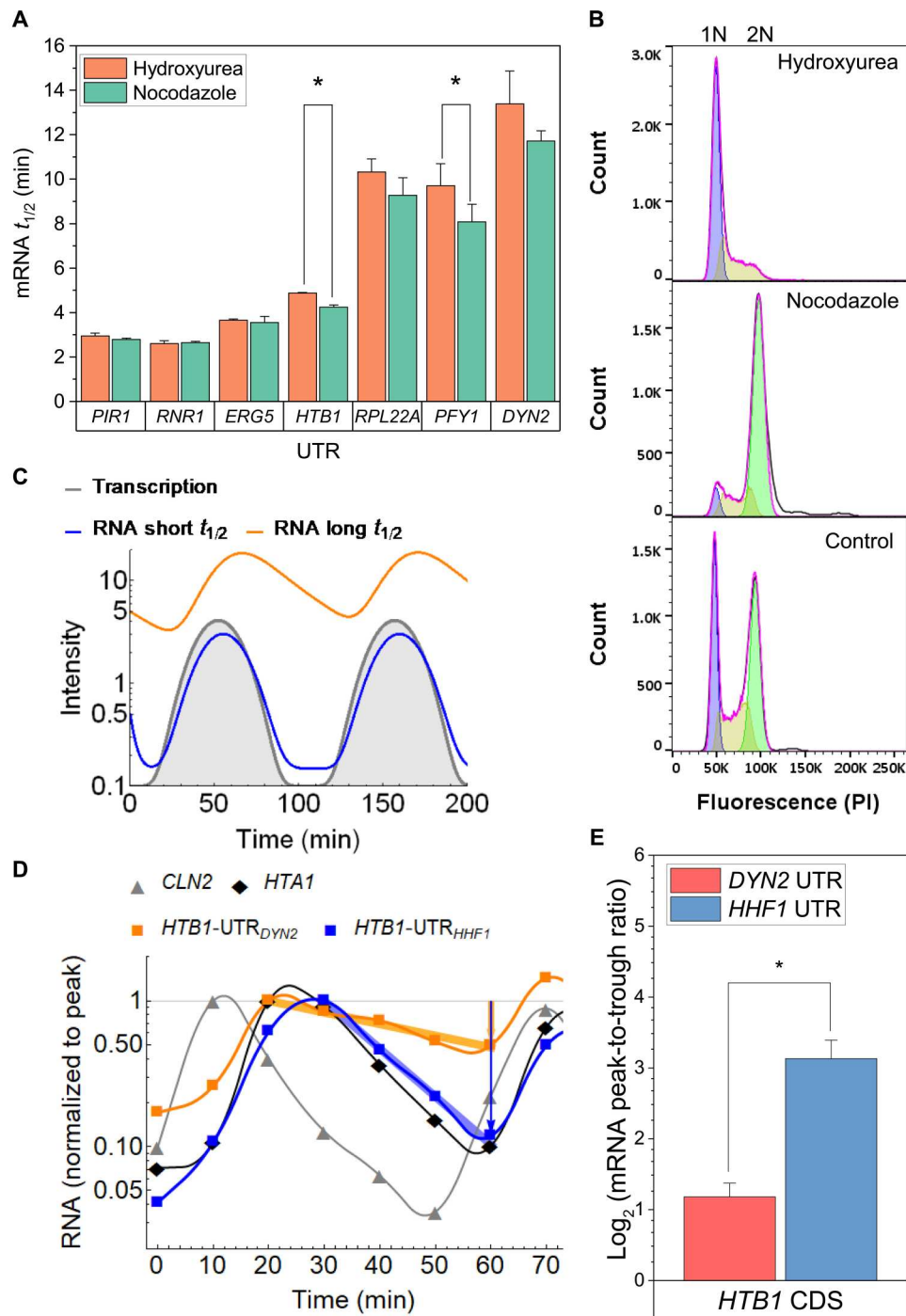
Fig. 4. Type II UTRs can increase the amplitude of oscillatory histone mRNA expression. (**A**) The half-life of mRNAs with the tandem reporter ORF flanked by the indicated UTRs was measured during cell cycle arrest in the S phase or G$_2$/M phase (2 hours after arrest with hydroxyurea or nocodazole, respectively). SE ($N = 3$). Significant differences were observed for *HTB1* ($P = 0.026$) and *PFY1* ($P = 0.018$) UTRs (t test). (**B**) The propidium iodide (PI) staining of cells indicates cellular DNA content (blue = 1N, green = 2N). Hydroxyurea: G$_1$/S = 98.8%; G$_2$/M = 0%. Nocodazole: G$_1$/S = 22.2%; G$_2$/M = 65.7%. Control: G$_1$/S = 56.8%; G$_2$/M = 40.7%. (**C**) mRNA concentrations calculated with a differential equation model when transcription is periodic (gray curves). The mRNAs have short (2 min) and long (20 min) half-lives. (**D**) Abundances of mRNA expressed from the *HTB1* CDS fused to the *HHF1* or *DYN2* 3'UTR in the cell cycle after a synchronization with α-factor. mRNA levels are normalized to their peak values in the first cell cycle. The expression of the endogenous *CLN2* and *HTA1* genes peak in the G$_1$ and S phases, respectively. The light orange and blue arrows at 60 min indicate the amplitude of the oscillations. The thick orange and blue lines between 20/30 and 60 min indicate exponential fits with a fourfold change in decay. (**E**) The amplitude of the indicated mRNAs measured as the peak-to-trough ratio ($N = 3$, paired t test, $P = 0.045$).
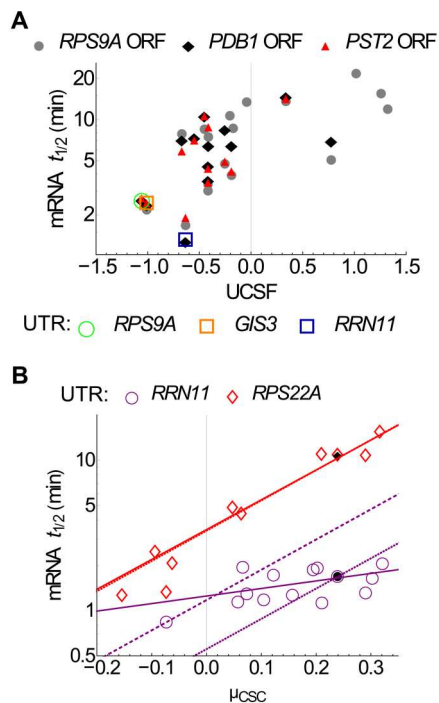
Fig. 5. Nonlinearity in the interaction of UTRs with codon optimality to modulate mRNA stability. (**A**) The half-life of chimeric mRNAs composed of the *RPS9A*, *PDB1*, and *PST2* CDSs and UTRs from genes with various UCSFs. The three most potent destabilizing UTRs fused to the *PDB1* CDS are indicated with open symbols. $r_s = 0.64$ (P value $= 5.6 \times 10^{-6}$, $N = 42$). (**B**) Half-life of chimeric mRNAs composed of the *RRN11* (UCSF = −0.63) and *RPS22A* (UCSF = −0.2) UTRs and CDSs of endogenous genes with the indicated mean codon stabilization, μ_{CSC}. The black filled circle and diamond denote endogenous, nonchimeric mRNAs. The dashed lines denote the function with proportional UTR effect $t_{1/2} = e^{a+b\mu_{csc}}e^{UCSF}$, whereas the full lines denote the function with a nonlinear interaction between UTR and CSC, $t_{1/2} = e^{a+b\beta(UTR)\mu_{csc}}e^{\alpha(UTR)}$. The two functions overlap for *RPS22A*. The dense and regular dashing denotes the original (UCSF) and fitted values of the linear function, respectively; none of them fits the *RRN11* data well. The following parameters were fitted in the nonlinear model: $\alpha = 0.32 \pm 0.13$, $\beta = 0.99 \pm 0.11$ ($N = 10$, $R^2 = 0.98$) for *RPS22A* and $\alpha = -0.57 \pm 0.11$, $\beta = 0.24 \pm 0.12$ ($N = 14$, $R^2 = 0.96$) for *RRN11*, indicating a strong destabilization by the *RRN11* UTR.

Efficient translation can occur even with short peptides, but the codon dependency of the translation only occurs above the critical CDS length

To measure translation of these short mRNAs, we used protein fragment complementation. Proteins that are C-terminally tagged with the nLCP can associate with the larger fragment of the Nanoluc luciferase, permitting exact protein quantification, even for short peptides (fig. S8, A and B, and Materials and Methods).

We measured first the translation quotient, the ratio of the steady-state luminescence to mRNA. By dividing the translation quotient of the high-CSC mRNA by that of the low-CSC mRNA, differential translation can be estimated. Overall, this estimate increases with the length of the coding sequence (Fig. 6A), recapitulating the observations with mRNA half-lives. To obtain a precise value of the translational efficiency, we measured the protein decay rates. Multiplying the translation quotient with the protein degradation rate yields the relative translation rate constant. First, we measured protein half-lives by shutting off gene expression.

The level of proteins declined rapidly after shutting off gene expression by doxycycline (fig. S8B), which was unexpected given that GFP and RFP are typically stable proteins. However, tagging of the full size tandem reporter with the smaller nanoluc fragment led to a disappearance of fluorescence (fig. S8D). These two observations suggest that the nLCP peptide destabilizes the protein. Therefore, we measured protein degradation rates upon addition of the translation inhibitor cycloheximide (CHX; fig. S8C). Most protein half-lives were short, ranging from 0.3 to 2 min. Smaller half-life differences can be also observed between the low- and high-CSC variants, which is possibly due to the differential folding of proteins translated from optimal and non-optimal codons (*22*, *23*).

Whereas the translation efficiency of mRNAS with short CDSs does not respond to codon optimality, mRNAs with 303- and 705-nt coding sequence showed significant codon optimality–dependent translation (Fig 6B), with around threefold higher translation in the high-CSC mRNAs. For comparison, only the mRNA with the 705-nt coding sequence displays a greater than 1.5-fold differential mRNA stability. Even short mRNAs can display very high codon-independent translation efficiency: The mRNAs with 204-nt coding sequences have higher translation than all longer mRNAs (Fig. 6B). Furthermore, the mRNA with the 354-nt coding sequence displays an inverse response to codon optimality, with a 0.6-fold decrease in translation efficiency. In summary, the translational efficiency of mRNAs responds to codon optimality not only above the threshold of differential mRNA stability: A variable response of translation can also be observed with coding sequence length below but close to the threshold. To characterize translation in more detail, we performed polysome profiling.

Polysome propensity explains differential mRNA stability

On the polysome profile, apart from the unbound fraction, mRNAs occupied by one to seven ribosomes can be distinguished (Fig. 7A). On average, 60% of the mRNAs in the *GFP-RFP* segment-nLCP (CDS)::*RPL41A* (UTR) series are occupied by one or more ribosome, which is slightly less than the genome-wide average of 71% (*24*), possibly due to a preponderance of short mRNAs in this series. The mRNAs were more enriched in monosomal fractions than in fractions containing either two, three, or more ribosomes. To assess the similarity of individual mRNAs according to their distribution in the polysome profile, we calculated the correlation matrix of their fractional abundances across the polysome profile. In the high-CSC series, the 204- and 303-nt CDS were the most similar to the mRNA with the 705-nt CDS (Fig. 7B); these mRNAs are more translated than the others (Fig. 6B). Thus, the polysome profiles do reflect the pattern of translation. Similar but less pronounced trends can be observed in the low-CSC series (fig. S9), possibly because translation is less variable in the low-CSC mRNAs (Fig. 6B).

A particularly high correlation was found between the *RPL41A* UTR–705 nLCP CDS and the *TUB1* UTR–369-nt CDS (sans nLCP) mRNAs (Fig. 7B), both of which display differential translation and mRNA stability (Fig. 6B). These mRNAs were rich in the mRNA fractions containing three and more ribosomes. Therefore, we quantified the polysome propensity of the individual mRNAs. Polysome propensity is the ratio of mRNAs in the polysome fractions containing three or more ribosomes to those in the monosome. The polysome propensity of the high-CSC series showed a
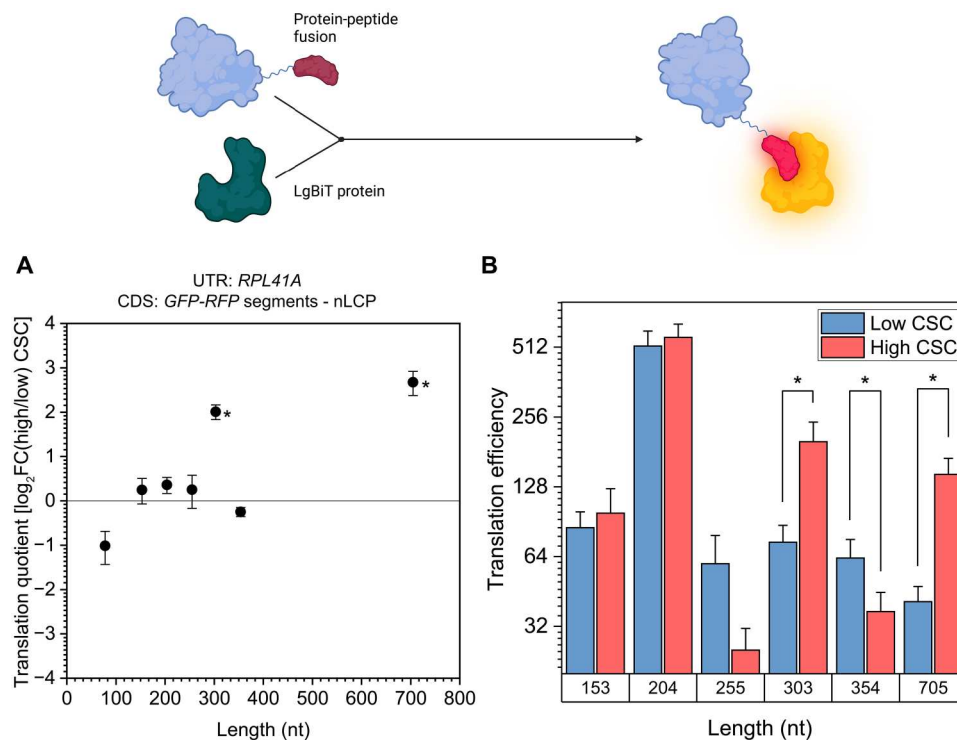
Fig. 6. CDS length dependence of translation of nLCP-tagged peptides and proteins. The scheme depicts complementation of the nLCP with the LgBiT subunit to reconstitute the functional nanoluciferase. For both panels, error bars denote the SE of the mean with $N = 4$. P values were calculated with paired t test. (**A**) The ratio of the translation quotients (i.e., translation quotient of high-CSC mRNAs/translation quotient of low-CSC mRNAs). P values < α = 0.05: 0.024 (303CDS) and 0.015 (705CDS). (**B**) The relative translation efficiencies of the high-CSC and low-CSC mRNAs of the nLCP-tagged constructs of various lengths. The translation efficiency is obtained by multiplying the translation quotients with the respective protein degradation rate. P values < α = 0.05: 0.029 (303CDS), 0.018 (354CDS), and 0.022 (705CDS).

marked dichotomy: All but the longest mRNA with the *RPL41A* UTR had a polysome propensity less than one, typically around 0.5 (Fig. 7C). In contrast, the 705-nt-long CDS displayed a high polysome propensity, around three. The 354-nt-long CDS with the *TUB1* UTR also had a similarly high polysome propensity in marked contrast to its counterpart with equal length, but having the *RPL41A* UTR, which does not display differential mRNA stability. Thus, the polysome propensity is a good metric that indicates differential mRNA stability.

To assess the number of endogenous mRNAs in the critical range of polysome propensity, RNA sequencing (RNA-seq) was performed. The mean fractional occupancy of the mRNAs by at least one ribosome is 0.83 across the transcriptome. The polysome propensity is highly, and inversely, correlated with the monosome to polysome (M:P) ratio, with the main difference between the two measures being that the latter includes also the disome fraction. The slope of the polysome propensity is somewhat steeper (fig. S10, A and B). The M:P ratios quantified in our study display a moderately good correlation with those in a prior study, but there are fewer mRNAs in monosome fraction in our dataset (fig. S10C) (*5*). In our dataset, most monosomal mRNAs are short, less than 1000 nt long ($N = 33$, polysome propensity < 1).

However, the above calculation may underestimate the number of mRNAs that have low polysome propensity and no differential stability. While the polysome propensity of high-CSC mRNAs is a good indicator of differential mRNA stability (Fig. 7C), the same metric is more ambiguous in the context of low-CSC mRNAs.

Low-CSC CDSs with lengths close to the threshold have typically higher polysome propensity than their high-CSC counterparts (fig. S9B). Many endogenous short mRNAs have a low codon optimality (data S2); thus, their high-CSC counterparts are expected to have lower polysome propensity (fig. S9B). For this reason, we created an expanded definition that includes mRNAs with a polysome propensity of up to 1.3, as long as their μ_{CSC} is less than 0.1. In this group (extrapolated monosomes, $N = 44$), two mRNAs have a CDS longer than 1000 nt, but both of them are subject to NMD (data S2). NMD targets have polysome profiles shifted toward monosomes (*5*). According to our conservative estimates (Fig. 7D), the half-lives of around 70 to 80 monosomal mRNAs are expected to have no or minimal response to changes in codon optimality.

We plotted mRNA stability ratios as a function of the polysome propensity of the endogenous mRNAs (Fig. 7E). There is an upsurge in differential stability as polysome propensity increases from two to three. The *HHF1* has a high polysome propensity (5.2; data S2) supporting the idea that type II UTRs accelerate mRNA degradation without changing the translational status.

DISCUSSION

We found that there are built-in thresholds of coding sequence length above which an mRNA gains the ability to respond to codon composition. The fact that differential mRNA stability and the polysome propensity also coincide suggests that the differential
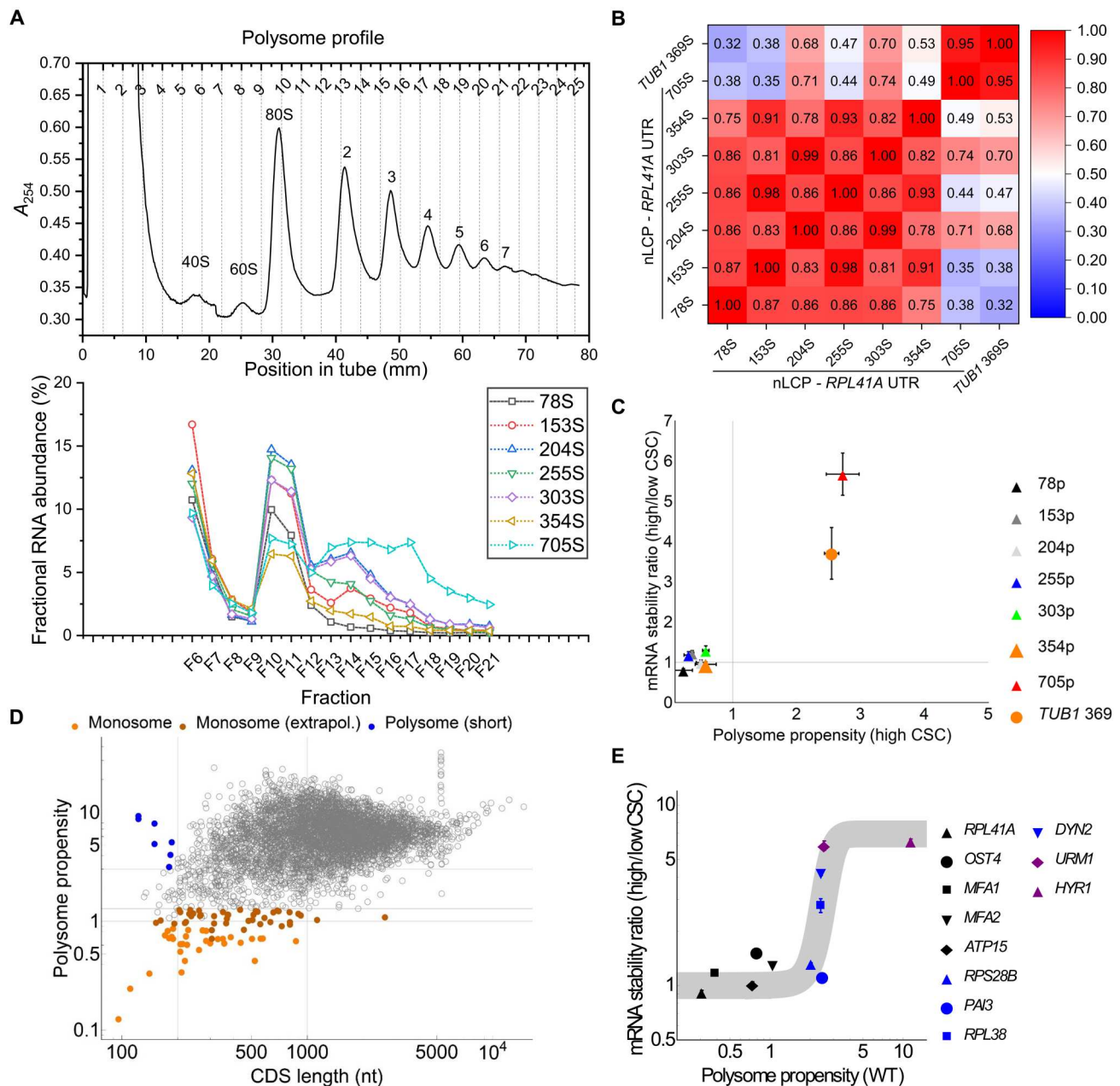
Fig. 7. Polysome profiling of the mRNAs. (**A**) The ribosome numbers are indicated at the absorbance peaks A_{254} as a function of position in the ultracentrifuge tube. The order number of the collected fractions is shown in the top axis. In the bottom, the fractional RNA abundances are shown in each fraction of the polysome profile. (**B**) The Spearman rank correlation of the mRNA amounts in the different fractions of polysome gradient. (**C**) The relationship between the polysome propensity and the mRNA stabilization ratio is shown in (B) (SE, $N = 3$). The CDS (*GFP-RFP* segments–nLCP):: UTR(*RPL41*) mRNAs are indicated as p. The mRNA consisting of the 369-nt-long CDS with *TUB1* UTR (without nLCP) and the mRNA with *RPL41A* UTR having a similar CDS length (354 nt) are shown in orange. (**D**) Genome-wide distribution of polysome propensity measured with RNA-seq. The classification of the monosomal and short polysomal mRNAs is described in Materials and Methods. (**E**) The mRNA stability ratio of the endogenous recoded genes (as in Fig. 2D) as a function of polysome propensity of endogenous mRNAs measured by qPCR. Genes with type II UTRs (*HHF1*) are omitted. $N = 2$. The curve is a guide to the eye.

response of mRNA degradation to codon optimality requires the cooperation of multiple ribosomes (Fig. 8). This is particularly evident in two mRNAs with coding sequences of similar lengths (354 and 369 nt) but with different UTRs; only the mRNA with the *TUB1* but not the *RPL41A* UTR displays high polysome propensity and differential stability.

The threshold length, which ranges between 200 and 700 nt, is reminiscent of the 5′ ramps detected in genome-wide analysis of ribosome footprinting. These 5′ ramps have a higher ribosome density over a length of around 200 codons (600 nt), a phenomenon conserved from yeast to humans (*25*). However, these ramps are present also in mRNAs with long coding sequences. Thus, ramps
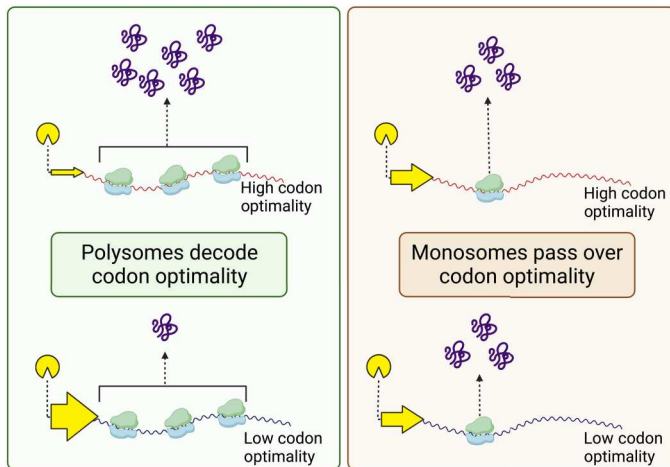
Fig. 8. Model of mRNA stability and polysome propensity. The left of the scheme shows that mRNAs with low and high codon optimality (low and high CSC) result in differential mRNA stability if mRNAs have high polysome propensity, which is typically associated with long CDSs. If the UTR (e.g., type I: *DYN2* versus *RPL41A*) or the encoded amino acids are changed, then the polysome propensity can drop and differential stability disappears even when the CDS length remains unchanged (left versus right). In this scheme, the translation is proportional to mRNA degradation, but this proportionality can be decoupled by type II UTRs.

and thresholds are distinct entities. It has been suggested that elongation is slower in these ramps irrespective of codon composition (*26*). It remains to be clarified whether the molecular mechanisms underlying the ramps and threshold lengths actually overlap.

Current evidence suggests that there are two distinct pathways that can link slow elongation to mRNA degradation pathways (*27*). The no-go pathway detects ribosomal stalls due to chemical damage of mRNAs such as oxidative damage, and once activated, the mRNA is degraded. Sequences rich in codons for positively charged residues can markedly slow down elongation (*28*). Even more, adjacent pairs of specific rare codons of arginine can mimic the no-go pathway. The resulting collision of upstream ribosomes leads to ubiquitination of the ribosome by Hel2. However, the main pathway that mediates mRNA decay due to non-optimal codons does not involve Hel2 and other proteins associated with the no go pathway, such as Syh1. The degradation triggered by non-optimal codons in general relies on a second pathway, initiated by a Not5-mediated deadenylation and decapping. Not5 senses the loading of ribosomes by tRNA, and in this way, it detects non-optimal codons. It remains to be determined how the mRNA threshold length and/or the cooperation of ribosomes enable functioning of this pathway (*29*).

Multiple mechanisms are known that can measure mRNA length. For example, NMD acts by measuring the distance between the premature stop codon and a downstream sequence (*30*). In some organisms, the number of introns or exon-junction density may act as a proxy for the coding sequence length in both NMD and mainstream mRNA degradation (*31–33*).

In the mRNAs we studied, the effect of codon optimality on mRNA stability (5.7-fold change; Fig. 2B) outweighs that on translation efficiency (3.7-fold change; Fig. 6A), implying an estimated overall 21-fold increase in protein levels due to the multiplicative interaction of these two posttranscriptional processes. It is important to note that the CSC is highly correlated with different measures of translation, but some of the codons behave differently with respect to translation and mRNA stability (*2, 6*). The divergence of the two processes in response to changes in codon optimality is also evidenced by the fact that the translation efficiency of short mRNAs is more variable compared to their half-life (Figs. 2B and 6A).

The threshold length for the differential mRNA stability can be tuned by UTRs. However, these type I UTRs differ from the type II UTRs, which are also capable of destabilizing an mRNA well above the threshold length. Because of the reduced mRNA stability ratio, it is more difficult to discern their effect on the threshold. Thus, type II UTRs primarily destabilize the mRNAs rather than modulate the threshold length. At the same time, they uncouple translation from mRNA stability. Many of the stable mRNAs encode ribosomal genes, in which case the coupling of translation with mRNA stability is advantageous because codon optimality amplifies gene expression multiplicatively satisfying the high demand for ribosomal proteins. Histone genes are expressed in the S-phase so that the newly replicated DNA can be immediately wrapped around histone proteins. The expression of the histone genes outside of the S-phase activates a checkpoint because it is detrimental to the cells (*10, 34*), and a rapid decline of histone concentration is desirable. Therefore, the coupling of translation with mRNA stability is disadvantageous for genes with dynamically changing expression. By uncoupling them, the UTRs of histone and other cell cycle genes enable dynamic mRNA oscillations with rapid transitions that are combined with efficient translation.

Short coding sequences are predominantly translated by monosomes (Fig. 7D). The rate of translation is believed to be inversely proportional to the monosome to polysome ratio (*35*). However, our results suggest that monosomal translation is not necessarily less efficient. In the monosomal mRNAs, there is an alternation of low and high translational intensity with the CDS length (Fig. 6B), a weak pattern that is reflected by the polysomal profile similarity (204 and 303 nt; Fig. 7B). The highest translation rate among all mRNAs was observed with a predominantly monosomal mRNA with solely 68 codons (i.e., 204 nucleotides; Fig. 6B). Translation of such short mRNAs may be facilitated by loops formed between the 3′ and 5′ ends of the mRNAs, and/or by specific proteins (*36, 37*). Other mechanisms favoring short coding sequences may also help; for example, a ribosomal protein becomes progressively dephosphorylated as the ribosome translates an mRNA, which can result in a higher average phosphorylation of mRNAs with short coding sequences (*38*).

Recent studies have revealed that RNAs traditionally classified as noncoding often have short noncanonical ORFs that result in the translation of peptides and short proteins across a broad range of organisms (*39–41*). Many of them have physiological functions, especially in cancer and immune response. Our results suggest that these short proteins and peptides can be translated efficiently. Even typical mRNAs can be subject to monosomal translation; mRNAs in synapses are more likely to be translated by monosomes than by polysomes in comparison to proteins translated in the cell bodies of neurons (*42*). Our findings support the idea that monosomal RNAs in the synapses can be efficiently translated, and the shift in the polysome propensity according to the subcellular localization may simply control the differential translation and differential mRNA stability.

MATERIALS AND METHODS
Calculation of the CSC, unified half-lives, and residuals
To assess the contribution of codons to mRNA half-lives, the CSC was calculated. CSC is the Pearson correlation coefficient (r) reflecting the correlation between the codon frequency and half-lives. In this work, the CSC was calculated from a dataset of mRNA half-lives measured using multiplexed gene control in cells grown in glucose at 30°C ($N = 82$ genes) (6) (data S1).

μ_{csc} is the average CSC of the codons of an mRNA

$$\mu_{csc} = \sum_{k=1}^{64} CSC_k f_k \tag{1}$$

To obtain robust estimates for mRNA half-lives on a genomic scale, we calculated the unified mRNA half-lives from multiple datasets. Datasets were obtained with transcriptional inhibition using the *rpb1-1* allele (3, 43), metabolic labeling (14, 44–47), and a combination of genomic run-on and RNA abundances (48, 49). Only genes that were present in at least two datasets were retained for the further calculations. The half-lives in each dataset were normalized by the respective median half-life. Three different averages were calculated, denoted as $t_{1/2}$(ALL), $t_{1/2}$(2010-2015), and $t_{1/2}$(ALL, MAD trimmed). The $t_{1/2}$(2010-2015) is calculated from the above datasets that were published between 2010 and 2015, whereas $t_{1/2}$(ALL) covers all of them, including two datasets obtained with recent methodologies of RNA processing after metabolic labeling (14, 47). $t_{1/2}$(MAD) was obtained by trimming with the help of the MAD metric to omit outliers. The median and the MAD were calculated from the normalized half-life for each gene. Half-lives obeying the relation median $- 2.5$MAD $< t_{1/2} <$ median $+ 2.5$MAD were retained. After this outlier removal, the average half-life was calculated for each gene, provided half-lives in at least three datasets remained available.

To assess the ultracodonic contributions to mRNA stability, the residual was calculated, which is the difference between the unified mRNA half-life and the mRNA half-life estimated from the μ_{csc} with linear regression

$$\ln[t_{1/2}(\text{unified})] = a + b\mu_{csc} + \text{residual} \tag{2}$$

a and b represent the linear regression coefficients.

We named this residual UCSF (data S1). Eq. 2 can be rearranged to express the unified half-life in terms of the codonic and ultracodonic contributions

$$t_{1/2}(\text{unified}) = e^{a + b\mu_{csc}} e^{\text{UCSF}} \tag{3}$$

Nonlinear models of the length and UTR dependence of half-lives
To model the length dependence, the half-life is decomposed into a length-dependent term $t_{1/2}(L)$ and the neutral half-life $t_{1/2}(0)$, which can be viewed as the limit of the half-life of an mRNA whose codon number approaches zero. Thus, $t_{1/2}(0)$ is largely determined by the UTR.

$$t_{1/2} = t_{1/2}(0) + t_{1/2}(L) \tag{4}$$

$t_{1/2}(L)$ is modeled as logistic function where L and L_C denote the actual length (independent variable) and the critical length of the

coding sequence, respectively

$$t_{1/2}(L) = \frac{V_n}{1 + e^{-k(L - L_c)}} \tag{5}$$

The parameter k determines the steepness of the sigmoid function. A hypothetical molecular mechanism that can be reduced into the above equation relies on reactions affecting the ribosome (see Supplementary Text) (26, 38).

In this work, we examined mRNAs with identical UTRs and CDSs of extreme codon optimality. Thus, V_n is the maximal or minimal half-life of low and high-CSC mRNAs, respectively, above the critical CDS length.

If the fitting of Eq. 5 did not constrain the parameter values sufficiently, we fitted directly the stability ratio function (Eq. 6) to the half-life ratios of the low- and high-CSC mRNAs.

$$\text{mRNA stability ratio } (L) = \frac{t_{1/2}(0, \text{ high CSC})}{t_{1/2}(0, \text{ low CSC})}$$
$$+ \frac{V_r}{1 + e^{-k(L - L_c)}}$$
$$= 1 + \frac{V_r}{1 + e^{-k(L - L_c)}} \tag{6}$$

In this simplified version, the threshold-length is defined for the overall codon optimality dependence of the half-life and not separately the low- and high-CSC mRNAs. Therefore, L_c as well as k are assumed to have equal values in the two series. V_r is the maximal mRNA stability ratio. This simplified equation can be used when the ratio of the half-lives converge to one in the limit of a zero-length CDS.

To model the UTR dependence of the mRNA half-lives, a linear model was used (Eqs. 2 and 3). Since the linear model does not fit well the CSC dependence of UTR action, a nonlinear model was devised. In the nonlinear model, the UTR effect is decomposed into a linear part (α), akin to the role of the UCSF as a residual (in Eq. 2), and a nonlinear part (β), which can diminish or neutralize the effect of codon composition, μ_{CSC}

$$\ln[V_n] = \alpha(\text{UTR}) + [a + b\mu_{csc}\beta(\text{UTR})] \tag{7}$$

This relation can be converted in the original linear time scale of half-lives

$$V_n = e^{a + b\beta(\text{UTR})\mu_{csc}} e^{\alpha(\text{UTR})} \tag{8}$$

Datasets and statistical analysis
For the analysis of association of UCSF with cell cycle expression and NMD, $\Delta upf3$ and unified cell cycle datasets were used, as follows. The $\Delta upf3$/WT half-life ratios were considered that were significant by twofold difference or q values as specified in the data source (14). The cell cycle periodicity corresponds to the $-\log_{10}$(periodicity P value) (50), and it reflects the RNA expression to recur at intervals as opposed to a constant RNA expression. The following datasets were used for the affinity capture by RNA binding proteins or RNA-protein interactions: the targets of Whi3 (51) and Puf4 (52). Enrichment analysis was performed with DAVID (53). In all statistical significance tests in this study, two-tailed tests were used.

Construction of plasmids and yeast strains

A tet-OFF system was used to drive the RNA transcription cassettes that includes the UTRs and sequences upstream and downstream of the UTRs to allow for transcriptional initiation and termination (6). The length of the sequences cloned upstream and downstream of the 5′ and 3′UTRs were determined as described earlier (6). The following types of transcription cassettes were cloned into pRS303 plasmids: the *GFP-RFP* tandem reporter flanked by different UTRs (table S1), shorter versions of the above coding sequence and chimeras of UTRs, and coding sequences of endogenous genes (table S2). The GFP is an enhanced GFP (eGFP), and the RFP sequence corresponds to mScarlet (54). Each tandem reporter sequence is classified as low- or high-CSC based on codon composition. Shorter ORFs were obtained from different parts of the coding sequences to allow multiplexing in the decay experiments. The 717-, 351-, 168-, 75-, and 30-bp fragments of the coding sequence were subcloned. To obtain the total ORF length, an 18 bp (comprising restriction sites, start and stop codons) has to be added. The nLCP constructs overlap in the C terminus, and are progressively extended toward the N terminus of the tandem reporter. The recoded genes were obtained by gene synthesis (GENEWIZ/Azenta).

The *WHI3* gene was deleted with a polymerase chain reaction (PCR) product in which the *URA3* ORF was flanked by sequences for recombination with the sequences upstream and downstream of the *WHI3* ORF in the genome.

For the recoding of the endogenous genes, a probabilistic weighting function was used to maximize or minimize μ_{csc}. The endogenous stop codons were retained. Codon swapping was performed on the CDS. Additional minor changes were made, for example, to remove restriction sites that interfere with the cloning or the linearization of plasmid for the integration. The endogenous introns were retained as well as the exonic codons in the neighborhood of the introns (*DYN2*).

All strains are isogenic with the BY4743 diploid *S. cerevisiae* cells. The gene constructs cloned into pRS303 plasmids were chromosomally integrated into the *his3* locus of the BY4742 yeast strain. Integrands with a single copy were selected with colony PCR. These MATα haploid strains were mated with the MATA haploid containing the tTA expression cassette integrated at the *leu2* locus.

Cells were grown overnight in synthetic complete synthetic medium (Complete Supplement: Formedium #DCS0019, Yeast Nitrogen Base: Formedium #CYN0410 in 2% raffinose and 0.005% glucose) at 30°C. The overnight cultures were refreshed to an optical density at 600 nm (OD_{600}) of 0.15 and grown at 30°C until they reached the mid-log phase, with final OD_{600} of 0.5, for further experiments.

Measurement of mRNA half-lives

Yeast cells expressing a gene of interest under the control of TET-off system were grown at 30°C in a shaker incubator until mid-log phase (OD_{600} of 0.5). Gene activation was halted by addition of doxycycline (Sigma-Aldrich #D9891) to a final concentration of 10 μg/ml, and samples were taken at specific time points to study the decay profile of the relevant mRNAs. The zero time point was taken to be just before the addition of doxycycline. Samples were collected in tubes containing absolute methanol (Sigma-Aldrich #32213) chilled on dry ice, in a volume ratio of 1:1. They were then spun in a centrifuge at 4°C for 10 min at 4000g. The supernatant was

removed completely, and the samples were stored at −80°C until lysis.

Lysis was carried out using the MPBio FastPrep bead lysis system and Lysing Matrix Y (MPBio #116960050-CF). RNA was extracted using RNeasy Mini kits (Qiagen #74104) following the relevant instructions. Reverse transcription was carried out on 1 μg of total RNA using SuperScript III (Thermo Fisher Scientific #18080044) using gene specific primers. RNA levels were quantified using quantitative PCR (qPCR; Roche LightCycler 480, KAPA SYBR Fast #KK4611), normalized to endogenous housekeeping genes for internal control (*TFC1* and *UBC6*) to obtain the relative amount mRNA.

An exponential decay function was fitted to the normalized RNA levels over time using Wolfram Mathematica to obtain mRNA half-lives. A 2-min gap was subtracted from the time at which the sample was collected to allow for the delay in gene deactivation by doxycycline. At least two measurement replicates were performed. All replicate measurements were performed on samples obtained from cultures grown on different days.

Measurement of protein half-life with protein fragment complementation

Genes were constructed to express peptides/proteins tagged on the C terminus with an nLCP tag (peptide 86: VSGWRLFKKIS) (55). Cells were grown until the mid-log phase. For protein half-life measurements, translation was stopped by addition of CHX (Thermo Fisher Scientific #357420050) at a final concentration of 100 μg/ml. Samples were collected in tubes containing absolute methanol (Sigma-Aldrich #32213) chilled on dry ice, in a volume ratio of 1:1. The 0′ time point was taken to be just before addition of CHX.

Cells were dissolved in a modified version of glass bead disruption buffer (56) [20 mM tris-HCl (pH 8.0), 10 mM $MgCl_2$, 1 mM EDTA, 5% glycerol, 1 mM dithiothreitol (DTT), 0.3 M ammonium sulfate, and 1× cOmplete EDTA free Protease Inhibitor (Sigma-Aldrich #COEDTAF-RO)/100 ml]. Cell suspensions were loaded into 1.5-ml microfuge tubes on benchtop shaker/incubator set at 4°C, and lysis was carried out with Zirconia/Silica beads (Biospec #11079105z). Fifteen cycles of interval shaking were carried out with each cycle consisting of 30 s shaking at 2000 rpm and 30 s resting periods. The tubes were then spun at 10,000g for 5′ to clarify the lysate.

Luminescence was measured using the Nano-Glo HiBiT Lytic Detection System (Promega #N3040). Fifty microliters of lysate was mixed with 50 μl of Nano-Glo HiBiT Lytic Reagent (which contains both the LgBiT protein, of which the nLCP is complement, and the luminescence substrate). Luminescence readings were measured in a multimode plate reader (Tecan Spark).

Protein half-lives were calculated by fitting the raw luminescence values to an exponential decay equation in Wolfram Mathematica.

Cell cycle synchronization

S. cerevisiae MAT A strains isogenic to BY4741A were transformed by 3′UTR replacement cassettes yielding *HTB1* CDS::*DYN2* UTR–*HIS3*(_pSYN109) and *HTB1* CDS::*HHF1* UTR–*HIS3*(_pSYN110) integrations into the endogenous sites in the chromosome. The corresponding strains (YSV574 and YSV575) were multiplexed and grown in YPAD medium at 30°C until the mid-log phase (OD_{600} = 0.4). Then, they were refreshed to an OD_{600} of 0.2, and α-factor (Sigma-Aldrich #T6901) was

added to a final concentration of 5 μg/ml. Cells were observed by light microscopy for the appropriate "schmoo" morphology, which signifies cell cycle arrest. Once >90% of the cells displayed this characteristic morphology (around 100 min after α-factor addition), they were released from the cell cycle arrest by passing the culture through a 0.45-μm cellulose acetate membrane filter (Sartorius) and by resuspending the residual cells in fresh YPAD medium (at 30°C but without α-factor). Samples were collected (in 50% methanol) every 10 min starting from the 0-min mark (defined as the moment before filtration) up until 90 min after release. The collected samples were processed as described in the "Measurement of mRNA half-lives" section.

Measurement of translation efficiency

The relative translational efficiency is the product of the protein decay rate constant (γ) and the translation quotient. The translation quotient is the ratio of the steady-state abundance of protein to that of the cognate RNA, where RNA and protein abundances are normalized to the total or specific species.

$$\text{Relative translational efficiency} = \gamma \cdot \text{Translation quotient}$$

$$= \gamma \frac{\langle \text{Protein} \rangle}{\langle \text{RNA} \rangle} \tag{9}$$

RNA isolation, reverse transcription, and qPCR were performed as previously described. For the measurement of the GFP-mScarlet mRNA, primers annealing to coding sequence were used. For the measurement the nLCP-tagged construct, the primers were designed to anneal to the nLCP coding region and the flanking 3′UTR. These abundances were normalized the *TFC1* and *UBC6* mRNAs.

The abundance of the GFP-mScarlet fusion protein was quantified by flow cytometry (BD LSRFortessa System). The Ex488_505LP_512/25-A filter was used for GFP and Ex561_600LP_610/20-A for mScarlet. FSC/SSC gating was applied to remove cell doublets.

Protein abundances of the nLCP-tagged constructs were quantified by the Nano-Glo HiBiT Lytic Detection System and normalized to the total protein concentration. The total protein concentration in the lysate was quantified with a Bradford assay (Thermo Fisher Scientific Pierce Detergent Compatible Bradford Assay Kit #23246) by measuring the absorbance at 595 nm (A595) on a multimode plate reader (Tecan Spark). All replicate measurements were performed on distinct samples obtained from cultures grown on different days.

Cell cycle arrest

Yeast strains were grown to mid-log phase (OD$_{600}$ = 0.5) and were treated with hydroxyurea (Sigma-Aldrich #H8627; final concentration: 200 mM) or nocodazole (Sigma-Aldrich #M1404; final concentration: 15 μg/ml) to arrest them in the S phase or the G$_2$-M phase, respectively (57). The arrest was allowed to reach completion by an incubation of 2 hours, and then doxycycline was added to shut off gene expression (as described in the "Measurement of mRNA half-lives" section). The progression toward cell cycle arrest was monitored by taking samples at different time points to measure DNA content in the cells. Samples were spun for 1 min at 15,000g in the microcentrifuge, and the supernatant was removed. Fixation was carried out with absolute ethanol, and then the cells were washed with distilled water. To remove RNA and protein, the samples were resuspended in 50 mM sodium citrate and treated with ribonuclease A [dissolved in STE buffer: 100 mM NaCl, 10 mM tris-HCl, and 1 mM EDTA (pH 8.0)] and Proteinase K at 50°C for 1 hour (58). Subsequently, propidium iodide (16 μg/ml; Sigma-Aldrich #81845) dissolved in 50 mM sodium citrate solution was added to stain the DNA, and fluorescence was measured with flow cytometry (LSR Fortessa) using the Ex561_600LP_610/20-A filter. Twenty thousand cells were measured. The flow cytometry data were analyzed using FlowJo v10.8 Software (BD Life Sciences). The percentage of cells in different parts of the cell cycle was derived using the Watson (pragmatic) model in their cell cycle toolbox.

Polysome profiling

Cells were collected by addition of the culture to 2 volumes of chilled medium (4°C) containing CHX (Thermo Fisher Scientific #357420050) at 1.5× (150 μg/ml). The culture was spun down at 4000g for 10 min in a centrifuge at 4°C. The supernatant was removed, and the pellet was immediately subjected to lysis. This CHX pretreatment serves to prevent ribosome runoff (59). The rapid cooling was used to prevent CHX-induced artifacts (25).

To start the cell lysis, cells were dissolved in 1× polysome lysis buffer (PLB) [20 mM tris-HCl (Thermo Fisher Scientific #AM9856), 10 mM MgCl$_2$ (Thermo Fisher Scientific #AM9530G), 1 mM DTT (Thermo Fisher Scientific #707265ML), CHX (100 μg/ml; Thermo Fisher Scientific #J66004-XF), 2 cOmplete EDTA free Protease Inhibitor (Sigma-Aldrich #COEDTAF-RO)/100 ml, the RNase inhibitor (RNasIN) (8 U/ml; Promega #N2611), and 1% (v/v) Triton X-100 (Fluka #93418)]. Lysis was carried out with Zirconia/Silica beads (Biospec #11079105z) with cell suspensions loaded in 1.5-ml microfuge tubes on benchtop shaker/incubator set at 4°C. Fifteen cycles of interval shaking was carried out with each cycle consisting of 30 s ON at 2000 rpm and 30 s OFF.

For the gradient, 10 and 50% (w/v) sucrose (Thermo Fisher Scientific #036508-30) solutions were prepared in 1× polysome gradient buffer (as PLB but without Triton X-100). The 10% sucrose was loaded on the centrifuge tubes [Beckman C14293/344059 Ultraclear 13.2 ml (compatible with SW41Ti rotor)]. With a 20-ml syringe attached to long cannula, the 50% solution was layered at the bottom. The tubes were then covered with caps (BioComp #105-414-1), and the gradient was formed by high angle rotation, using the 10 to 50% short cap (rate zonal) protocol in the BioComp Gradient Station machine.

To assess the volume of the cell lysate to be loaded, A$_{254}$ was measured, and a total of 10 to 50 A$_{260}$ units was loaded onto the 10 to 50% sucrose gradient. Ultracentrifugation was carried out with a SW41Ti rotor (swing bucket) at 40000 rpm for 2 hours at 4°C. The polysome profile was generated using the BioComp Gradient Station machine, and 25 different fractions (450 μl each) corresponding to different lengths in the centrifuge tube were collected. RNA from each fraction was purified by acid Phenol : Chloroform : Isoamyl Alcohol :: 25 : 24 : 1. Precipitation was carried out with one volume of isopropanol at 4°C for 30 min to 1 hour with 2 μl of GlycoBlue (Thermo Fisher Scientific #AM9516) as coprecipitant. RNA was reconstituted with 20 μl of nuclease-free water (Thermo Fisher Scientific #AM9932) containing RNasIN (Promega #N2611) at 1 μL/ml (40 U/ml).

Reverse transcription was carried out subsequently with Super-Script IV (Thermo Fisher Scientific #18090200), using random hex-amers (Promega #C1181) with the ezDNase (DNase) pretreatment (Thermo Fisher Scientific # 11766051) as per the protocol, and qPCR was then carried out (Roche LightCycler 480, KAPA SYBR Fast #KK4611).

Analysis of polysome profiles by qPCR
The RNA intensities were calculated in each fraction (i) and then represented as the percentage of total RNA intensity (for that species) across all fractions.

$$\text{Fractional abundance of RNA (\% of total)} = \text{RNA}_i(\%)$$

$$= \frac{\text{RNA}_i}{\sum_i \text{RNA}_i} \cdot 100\%$$

The RNA occupancy was calculated by adding up the RNA in-tensities starting from the monosome fraction and ending with the fraction one above the seven-ribosomal peak.

$$\text{RNA occupancy (\%)} = \sum_{i=\text{RP}_1}^{\text{RP}_7+1} \text{RNA}_i 100\%$$

The polysome propensity was calculated as the ratio of the frac-tional RNA abundance in the polysome to the fractional RNA abun-dance in the monosome. Both the polysome and monosome fractions were background-corrected, and the background correc-tion was scaled according to the number of fractions being com-bined, the polysome fraction being composed of $N_p = 8$ fractions, and the monosome of $N_m = 2$ fractions, respectively. Background was defined as the average of the RNA intensities in the first, last but one (24th) and last (25th) fraction. $\text{Bg} = \sum_{i \in \{1,24,25\}} \text{RNA}_i$

$$\text{Polysome propensity} = \frac{\sum_{x=i(\text{RP}_2)+1}^{n=i(\text{RP}_7)} \text{RNA}_i - N_p \cdot \text{Bg}}{\sum_{x \in i(\text{RP}_1)} \text{RNA}_i - N_m \cdot \text{Bg}}$$

The i denotes the index number of the fraction. RP_1 is the first ribosomal peak (i.e., the monosome), and RP_7 is the seventh ribo-somal peak, making $(\text{RP}_7 + 1)$ the fraction right after the one cor-responding to seven ribosomes. $N_p = [i(\text{RP}_7) - i(\text{RP}_2) + 1]$, $N_m = i(\text{RP}_1)$.

RNA-seq and data processing
Two biological replicates of polysome profiling (R2 and R3) were processed for RNA sequencing. The fractions 1 to 5 (free RNA) were pooled into a single tube. Fractions 6 to 23 and 25 were pro-cessed separately. An in vitro–transcribed spike-in RNA was added to the total RNA to serve as a volumetric control. To remove any remaining cellular DNA, the RNA was treated with DNase (ezDNase, Invitrogen #11766051). Ribosomal RNA was depleted with QIAseq FastSelect–rRNA (Qiagen). cDNA library was pre-pared with Stranded SMART-Seq (Takara) by random priming. Ten and 13 cycles of amplification were performed in the first and second rounds, respectively. Primer dimers were removed by the ProNex Size-Selective Purification System (Promega), using a 1.33 chemistry ratio. Barcoded libraries were sequenced in Novaseq6000 (Illumina) flow cell type S1 with a sequencing by syn-thesis 100 cycle kit resulting in single-end reads of 100-bp length.

Single-end sequence reads were trimmed for adaptor sequences using TrimGalore (v0.6.5) with *--illumina* parameter. Trimmed se-quence reads were mapped, and transcript per million (TPM) values were obtained with Salmon (v1.0.0) (*60*). Specifically, Salmon's index was created from National Center for Biotechnology Informa-tion (NCBI)'s reference transcriptome (S288C, assembly R64). TPM quantification was performed with *salmon quant* command with the following parameters: *--validateMappings --seqBias −gcBias*.

Analysis of the RNA-seq data for polysome profiling
The TPM values were divided by the spike in-RNA to obtain RNA concentrations (of arbitrary units). To remove genes with high mea-surement noise, especially those with low expression, the following steps were undertaken. Genes with more than seven fractions with zero counts were removed; these were mostly noncoding RNAs. Furthermore, genes were filtered out when the polysome propensity has coefficient of variation (CV) larger than 0.8. Genes with a total RNA concentration less than 0.002 were separated into a group of genes with low expression. This group was not included in the genome-wide analysis of polysome propensity. The protein encod-ing gene with the highest expression, *RPS29B*, has an average RNA concentration of 72 (arbitrary units). The 5150 remaining genes cover thus around a 4×10^4–fold dynamic range in RNA expression.

Supplementary Materials
This PDF file includes:
Supplementary Text
Figs. S1 to S10
Tables S1 and S2
Legends for data S1 to S5

Other Supplementary Material for this manuscript includes the following:
Data S1 to S5

REFERENCES AND NOTES
1. F. Hia, O. Takeuchi, The effects of codon bias and optimality on mRNA and protein reg-ulation. *Cell. Mol. Life Sci.* **78**, 1909–1928 (2021).
2. R. L. Carneiro, R. D. Requiao, S. Rossetto, T. Domitrovic, F. L. Palhano, Codon stabilization coefficient as a metric to gain insights into mRNA stability and codon bias and their re-lationships with translation. *Nucleic Acids Res.* **47**, 2216–2228 (2019).
3. V. Presnyak, N. Alhusaini, Y. H. Chen, S. Martin, N. Morris, N. Kline, S. Olson, D. Weinberg, K. E. Baker, B. R. Graveley, J. Coller, Codon optimality is a major determinant of mRNA stability. *Cell* **160**, 1111–1124 (2015).
4. J. Cheng, K. C. Maier, Z. Avsec, P. Rus, J. Gagneur, *Cis*-regulatory elements explain most of the mRNA stability variation across genes in yeast. *RNA* **23**, 1648–1659 (2017).
5. E. E. Heyer, M. J. Moore, Redefining the translational status of 80S monosomes. *Cell* **164**, 757–769 (2016).
6. V. Jaquet, S. Wallerich, S. Voegeli, D. Túrós, E. C. Viloria, A. Becskei, Determinants of the temperature adaptation of mRNA degradation. *Nucleic Acids Res.* **50**, 1092–1110 (2022).
7. B. Ho, A. Baryshnikova, G. W. Brown, Unification of protein abundance datasets yields a quantitative saccharomyces cerevisiae proteome. *Cell Syst.* **6**, 192–205.e3 (2018).
8. C. E. Gamble, C. E. Brule, K. M. Dean, S. Fields, E. J. Grayhack, Adjacent codons act in concert to modulate translation efficiency in yeast. *Cell* **166**, 679–690 (2016).
9. G. Badis, C. Saveanu, M. Fromont-Racine, A. Jacquier, Targeted mRNA degradation by deadenylation-independent decapping. *Mol. Cell* **15**, 5–15 (2004).
10. A. Gunjan, A. Verreault, A Rad53 kinase-dependent surveillance mechanism that regulates histone protein levels in S. cerevisiae. *Cell* **115**, 537–549 (2003).
11. S. U. Khan, M. U. Khan, M. F. Kalsoom, M. I. Khan, S. Gao, A. Unar, M. Zubair, M. Bilal, Mech-anisms of gene regulation by histone degradation in adaptation of yeast: An overview of recent advances. *Arch. Microbiol.* **204**, 287 (2022).

12. C. F. Kurat, J. Recht, E. Radovani, T. Durbic, B. Andrews, J. Fillingham, Regulation of histone gene transcription in yeast. *Cell. Mol. Life Sci.* **71**, 599–613 (2014).

13. A. T. Belew, V. M. Advani, J. D. Dinman, Endogenous ribosomal frameshift signals operate as mRNA destabilizing elements through at least two molecular pathways in yeast. *Nucleic Acids Res.* **39**, 2799–2808 (2011).

14. H. Alalam, J. A. Zepeda-Martinez, P. Sunnerhagen, Global SLAM-seq for accurate mRNA decay determination and identification of NMD targets. *RNA* **28**, 905–915 (2022).

15. K. Leppek, R. Das, M. Barna, Functional 5′ UTR mRNA structures in eukaryotic translation regulation and how to find them. *Nat. Rev. Mol. Cell Biol.* **19**, 158–174 (2018).

16. S. Huch, T. Nissan, Interrelations between translation and general mRNA degradation in yeast. *Wiley Interdiscip. Rev. RNA* **5**, 747–763 (2014).

17. A. Becskei, S. Rahaman, The life and death of RNA across temperatures. *Comput. Struct. Biotechnol. J.* **20**, 4325–4336 (2022).

18. G. Hanson, J. Coller, Codon optimality, bias and usage in translation and mRNA decay. *Nat. Rev. Mol. Cell Biol.* **19**, 20–30 (2018).

19. A. Becskei, M. G. Boselli, A. van Oudenaarden, Amplitude control of cell-cycle waves by nuclear import. *Nat. Cell Biol.* **6**, 451–457 (2004).

20. E. D. Wong, S. R. Miyasato, S. Aleksander, K. Karra, R. S. Nash, M. S. Skrzypek, S. Weng, S. R. Engel, J. M. Cherry, Saccharomyces genome database update: Server architecture, pan-genome nomenclature, and external resources. *Genetics* **224**, iyac191 (2023).

21. Y. Cai, B. Futcher, Effects of the yeast RNA-binding protein Whi3 on the half-life and abundance of CLN3 mRNA and other targets. *PLOS ONE* **8**, e84630 (2013).

22. S. Pechmann, J. Frydman, Evolutionary conservation of codon optimality reveals hidden signatures of cotranslational folding. *Nat. Struct. Mol. Biol.* **20**, 237–243 (2013).

23. E. Esposito, D. E. Weidemann, J. M. Rogers, C. M. Morton, E. K. Baybay, J. Chen, S. Hauf, Mitotic checkpoint gene expression is tuned by codon usage bias. *EMBO J.* **41**, e107896 (2022).

24. Y. Arava, Y. Wang, J. D. Storey, C. L. Liu, P. O. Brown, D. Herschlag, Genome-wide analysis of mRNA translation profiles in Saccharomyces cerevisiae. *Proc. Natl. Acad. Sci. U.S.A.* **100**, 3889–3894 (2003).

25. P. Sharma, J. Wu, B. S. Nilges, S. A. Leidel, Humans and other commonly used model organisms are resistant to cycloheximide-mediated biases in ribosome profiling experiments. *Nat. Commun.* **12**, 5094 (2021).

26. D. E. Weinberg, P. Shah, S. W. Eichhorn, J. A. Hussmann, J. B. Plotkin, D. P. Bartel, Improved ribosome-footprint and mRNA measurements provide insights into dynamics and regulation of yeast translation. *Cell Rep.* **14**, 1787–1799 (2016).

27. A. J. Veltri, K. N. D'Orazio, L. N. Lessen, R. Loll-Krippleber, G. W. Brown, R. Green, Distinct elongation stalls during translation are linked with distinct pathways for mRNA degradation. *eLife* **11**, e76038 (2022).

28. S. E. Leininger, J. Rodriguez, Q. V. Vu, Y. Jiang, M. S. Li, C. Deutsch, E. P. O'Brien, Ribosome elongation kinetics of consecutively charged residues are coupled to electrostatic force. *Biochemistry* **60**, 3223–3235 (2021).

29. R. Buschauer, Y. Matsuo, T. Sugiyama, Y. H. Chen, N. Alhusaini, T. Sweet, K. Ikeuchi, J. Cheng, Y. Matsuki, R. Nobuta, A. Gilmozzi, O. Berninghausen, P. Tesina, T. Becker, J. Coller, T. Inada, R. Beckmann, The Ccr4-Not complex monitors the translating ribosome for codon optimality. *Science* **368**, eaay6912 (2020).

30. T. A. Hoek, D. Khuperkar, R. G. H. Lindeboom, S. Sonneveld, B. M. P. Verhagen, S. Boersma, M. Vermeulen, M. E. Tanenbaum, Single-molecule imaging uncovers rules governing nonsense-mediated mRNA decay. *Mol. Cell* **75**, 324–339.e11 (2019).

31. C. Zhao, T. Hamilton, Introns regulate the rate of unstable mRNA decay. *J. Biol. Chem.* **282**, 20230–20237 (2007).

32. H. F. Wang, L. Feng, D. K. Niu, Relationship between mRNA stability and intron presence. *Biochem. Biophys. Res. Commun.* **354**, 203–208 (2007).

33. N. Spies, C. B. Burge, D. P. Bartel, 3′ UTR-isoform choice has limited influence on the stability and translational efficiency of most mRNAs in mouse fibroblasts. *Genome Res.* **23**, 2078–2090 (2013).

34. C. Bruhn, A. Ajazi, E. Ferrari, M. C. Lanz, R. Batrin, R. Choudhary, A. Walvekar, S. Laxman, M. P. Longhese, E. Fabre, M. B. Smolka, M. Foiani, The Rad53(CHK1/CHK2)-Spt21(NPAT) and Tel1(ATM) axes couple glucose tolerance to histone dosage and subtelomeric silencing. *Nat. Commun.* **11**, 4154 (2020).

35. M. Pospisek, L. Valasek, Polysome profile analysis–Yeast. *Methods Enzymol.* **530**, 173–181 (2013).

36. Q. Vicens, J. S. Kieft, O. S. Rissland, Revisiting the closed-loop model and the nature of mRNA 5′-3′ communication. *Mol. Cell* **72**, 805–812 (2018).

37. M. K. Thompson, M. F. Rojas-Duran, P. Gangaramani, W. V. Gilbert, The ribosomal protein Asc1/RACK1 is required for efficient translation of short mRNAs. *eLife* **5**, e11154 (2016).

38. J. Bohlen, M. Roiuk, A. A. Teleman, Phosphorylation of ribosomal protein S6 differentially affects mRNA translation based on ORF length. *Nucleic Acids Res.* **49**, 13062–13074 (2021).

39. S. Plaza, G. Menschaert, F. Payre, In search of lost small peptides. *Annu. Rev. Cell Dev. Biol.* **33**, 391–416 (2017).

40. P. Patraquim, E. G. Magny, J. I. Pueyo, A. I. Platero, J. P. Couso, Translation and natural selection of micropeptides from long non-canonical RNAs. *Nat. Commun.* **13**, 6515 (2022).

41. H. W. Wu, E. Fajiculay, J. F. Wu, C. C. S. Yan, C. P. Hsu, S. H. Wu, Noise reduction by upstream open reading frames. *Nat. Plants* **8**, 474–480 (2022).

42. A. Biever, C. Glock, G. Tushev, E. Ciirdaeva, T. Dalmay, J. D. Langer, E. M. Schuman, Monosomes actively translate synaptic mRNAs in neuronal processes. *Science* **367**, eaay4991 (2020).

43. I. Gupta, S. Clauder-Münster, B. Klaus, A. I. Järvelin, R. S. Aiyar, V. Benes, S. Wilkening, W. Huber, V. Pelechano, L. M. Steinmetz, Alternative polyadenylation diversifies posttranscriptional regulation by selective RNA-protein interactions. *Mol. Syst. Biol.* **10**, 719 (2014).

44. C. Miller, B. Schwalb, K. Maier, D. Schulz, S. Dümcke, B. Zacher, A. Mayer, J. Sydow, L. Marcinowski, L. Dölken, D. E. Martin, A. Tresch, P. Cramer, Dynamic transcriptome analysis measures rates of mRNA synthesis and decay in yeast. *Mol. Syst. Biol.* **7**, 458 (2011).

45. M. Sun, B. Schwalb, D. Schulz, N. Pirkl, S. Etzold, L. Larivière, K. C. Maier, M. Seizl, A. Tresch, P. Cramer, Comparative dynamic transcriptome analysis (cDTA) reveals mutual feedback between mRNA synthesis and degradation. *Genome Res.* **22**, 1350–1359 (2012).

46. B. Neymotin, R. Athanasiadou, D. Gresham, Determination of in vivo RNA kinetics using RATE-seq. *RNA* **20**, 1645–1652 (2014).

47. A. Chappleboim, D. Joseph-Strauss, O. Gershon, N. Friedman, Transcription feedback dynamics in the wake of cytoplasmic mRNA degradation shutdown. *Nucleic Acids Res.* **50**, 5864–5880 (2022).

48. A. Baudrimont, S. Voegeli, E. C. Viloria, F. Stritt, M. Lenon, T. Wada, V. Jaquet, A. Becskei, Multiplexed gene control reveals rapid mRNA turnover. *Sci. Adv.* **3**, e1700006 (2017).

49. V. Pelechano, S. Chavez, J. E. Perez-Ortin, A complete set of nascent transcription rates for yeast genes. *PLOS ONE* **5**, e15442 (2010).

50. A. Santos, R. Wernersson, L. J. Jensen, Cyclebase 3.0: A multi-organism database on cell-cycle regulation and phenotypes. *Nucleic Acids Res.* **43**, D1140–D1144 (2015).

51. K. J. Holmes, D. M. Klass, E. L. Guiney, M. S. Cyert, Whi3, an S. cerevisiae RNA-binding protein, is a component of stress granules that regulates levels of its target mRNAs. *PLOS ONE* **8**, e84060 (2013).

52. C. P. Lapointe, M. A. Preston, D. Wilinski, H. A. J. Saunders, Z. T. Campbell, M. Wickens, Architecture and dynamics of overlapped RNA regulatory networks. *RNA* **23**, 1636–1647 (2017).

53. B. T. Sherman, M. Hao, J. Qiu, X. Jiao, M. W. Baseler, H. C. Lane, T. Imamichi, W. Chang, DAVID: A web server for functional enrichment analysis and functional annotation of gene lists (2021 update). *Nucleic Acids Res.* **50**, W216–W221 (2022).

54. D. S. Bindels, L. Haarbosch, L. van Weeren, M. Postma, K. E. Wiese, M. Mastop, S. Aumonier, G. Gotthard, A. Royant, M. A. Hink, T. W. J. Gadella Jr., mScarlet: A bright monomeric red fluorescent protein for cellular imaging. *Nat. Methods* **14**, 53–56 (2017).

55. A. S. Dixon, M. K. Schwinn, M. P. Hall, K. Zimmerman, P. Otto, T. H. Lubben, B. L. Butler, B. F. Binkowski, T. Machleidt, T. A. Kirkland, M. G. Wood, C. T. Eggers, L. P. Encell, K. V. Wood, NanoLuc complementation reporter optimized for accurate measurement of protein interactions in cells. *ACS Chem. Biol.* **11**, 400–408 (2016).

56. B. Dunn, C. R. Wobbe, Preparation of protein extracts from yeast. *Curr. Protoc. Mol. Biol.* **Chapter 13**, Unit13.13 (2001).

57. A. P. Rosebrock, Synchronization and arrest of the budding yeast cell cycle using chemical and genetic methods. *Cold Spring Harb. Protoc.* **2017**, pdb.prot088724 (2017).

58. H. Zhang, W. Siede, Analysis of the budding yeast Saccharomyces cerevisiae cell cycle by morphological criteria and flow cytometry. *Methods Mol. Biol.* **241**, 77–91 (2004).

59. N. T. Ingolia, J. A. Hussmann, J. S. Weissman, Ribosome profiling: Global views of translation. *Cold Spring Harb. Perspect. Biol.* **11**, a032698 (2019).

60. R. Patro, G. Duggal, M. I. Love, R. A. Irizarry, C. Kingsford, Salmon provides fast and bias-aware quantification of transcript expression. *Nat. Methods* **14**, 417–419 (2017).

material transfer agreement. Requests for the tTA plasmid should be submitted to Addgene (www.addgene.org) plasmid #122932.

Science Advances

Polysome propensity and tunable thresholds in coding sequence length enable differential mRNA stability

Sayanur Rahaman, Simone Faravelli, Sylvia Voegeli, and Attila Becskei

View the article online
https://www.science.org/doi/10.1126/sciadv.adh9545
Permissions
https://www.science.org/help/reprints-and-permissions

Use of this article is subject to the Terms of service